**Impact Factor 3.1**
**Q2**

Computational Biology and Chemistry 124 (2026) 109080

Contents lists available at ScienceDirect

Computational Biology and Chemistry

journal homepage: www.elsevier.com/locate/cbac

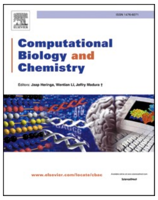

# Computational and experimental insights into quinazoline derivatives: Targeting HOTAIR for therapeutic intervention in breast cancer

Ali M. Alqahtani [a], Taha Alqahtani [a], Stalin Arulsamy [b], Swati Mayur Keny [c], Malarkodi Velraj [d], Kumarappan Chidambaram [a,*], Panneerselvam Theivendren [e,*]

[a] *Department of Pharmacology, College of Pharmacy, King Khalid University, Abha 62529, Saudi Arabia*
[b] *Department of Pharmaceutical Chemistry, Lovely Professional University, Jalandhar - Delhi, Grand Trunk Rd, Phagwara, Punjab 144411, India*
[c] *Department of Pharmaceutics, PES's Rajaram and Tarabai Bandekar College of Pharmacy, Ponda, Goa 403401, India*
[d] *Department of Pharmacognosy, School of Pharmaceutical Sciences, Vels Institute of Science, Technology & Advanced Studies, Pallavaram, Chennai, Tamil Nadu 600117, India*
[e] *Department of Pharmaceutical Chemistry & Analysis, School of Pharmaceutical Sciences, Vels Institute of Science, Technology & Advanced Studies, Pallavaram, Chennai, Tamil Nadu 600117, India*

## ARTICLE INFO

*Keywords:*
Quinazoline derivatives
HOTAIR
Breast cancer
Molecular docking
$IC_{50}$
Cytotoxicity
ADMET analysis

## ABSTRACT

Breast cancer which is the major cause of cancer deaths needs further innovative treatment methods to curb the weaknesses of the existing treatment methods. Quinazoline derivatives with an anticancer potential that seems to be highly promising are suggested to be used as targeted therapy in breast cancer. This paper explores the pharmacological role of 5,6,7,8-tetrahydroquinazoline derivatives in relation to the molecular interactions with HOTAIR (HOX transcript antisense intergenic RNA) which is a critical role in cancer metastasis. Computational studies such as molecular docking, molecular dynamics simulation was used in the research to evaluate binding affinity between identified quinazoline derivates and HOTAIR. Docking scores of the studied 25 compounds are between −7.4 to −9.4 kcal/mol with P14 demonstrating the best binding activity at −9.4 kcal/mol. Subsequent molecular dynamics simulations showed the structural stability of the complex between HOTAIR and P14 with a root mean square deviation (RMSD) range between 1.04 and 1.05 Å, the binding of the ligands to the RNA is also stable. MTT assays showed a dose-dependent reduction in the viability of the cells due to the cytotoxicity of the compounds in an in vitro setting. The obtained $IC_{50}$ results show that P14 was cytotoxic, given the obtained result of 57.73 μM. ADMET analysis revealed that P14 had decent bioavailability potential, but put certain concerns on toxicity, which has to be addressed by further in vitro and in vivo testing. These findings support the idea that quinazoline compounds and especially P14 have potential as therapeutic drugs against HOTAIR-mediated breast cancer and need to be investigated using preclinical models.

## 1. Introduction

Cancer as a global health crisis, continues to be one of the leading causes of mortality worldwide as new cases of cancer are diagnosed by millions of people every year. Breast cancer is the most wide-spread form of cancer (both in the case of women and in unusual circumstances, the case of men, who develop the disease). Breast cancer rates are growing consistently, and this issue has become one of the top priorities in the sphere of contemporary oncology. It is marked by the unregulated division of cells in the mammary mass which may extend to the other body parts through metastasis. The severity of the disease is the fact that it is difficult to detect at its early stages which mostly results in late diagnosis and low survival chances (Chandrasekaran et al., 2023; Dinesh et al., 2025; Kunjiappan et al., 2021).

Breast cancer is heterogeneous and consists of dissimilar subtypes which vary in molecular signatures, behaviours and treatment responses. Breast cancer is a major challenge even though there has been improvement in early identification and treatment interventions such as surgery, chemotherapy, radiotherapy, and hormonal therapies (Ma et al., 2020; Zeng et al., 2023). Detection of the disease early by using mammography and frequent self-exams can also help increase survival of the disease, although there are still gaps in the ability to develop specific therapies to treat resistant and metastatic type of the disease. The frequent appearance of side effects under current treatment

---

* Corresponding authors.
*E-mail addresses:* kumarappan@kku.edu.sa (K. Chidambaram), panneerselvam.sps@vistas.ac.in (P. Theivendren).

https://doi.org/10.1016/j.compbiolchem.2026.109080
Received 21 October 2025; Received in revised form 13 April 2026; Accepted 16 April 2026

regimens demonstrates the increased necessity in the development of new ways of treatment (Pandian et al., 2022; Radhakrishna et al., 2024; Ramesh et al., 2023).

Spanning the numerous potential solutions to breast cancer is the possibility of more preliminary leads; one of which is quinazoline and derivatives (Xing et al., 2024; Zhao et al., 2024). The bicyclic compound, quinazoline has received attention and it is noted that it possesses various pharmacological uses but mostly as an anti-cancer agent. Its derivatives have had some potential of hindering the growth of different types of cancer cell lines such as breast cancer due to its ability of contracting essential molecular pathways regulating cell proliferation, apoptosis as well as angiogenesis (Yuan et al., 2025). Quinazoline compounds have been explored to interfere with signaling pathways like EGFR and the vascular endothelial growth factor receptor VEGFR, through which they have a crucial role to play in tumor growth and metastasis. In this way, quinazoline derivatives are able to offer viable mode of treatment to patients with resistant breast cancer (Selvaraj et al., 2022; Surya et al., 2024; Theivendren et al., 2025a, 2025a, 2025b).

The discoveries about long non-coding RNAs (lncRNAs), including HOTAIR (HOX transcript antisense intergenic RNA), are also a promising direction of research when it comes to breast cancer. HOTAIR is identified as strong upregulated in breast cancer and it is related to the tumor development, metastasis and unfavourable prognosis. It carries out regulation on gene expression in interacting with chromatin remodelling complexes and alteration of the expression of oncogenes. The role of HOTAIR in breast cancer has created new modalities of treatment and researchers are working to create inhibitors of HOTAIR as one of the possible treatments (Cantile et al., 2020; Liguori et al., 2021). Through the mechanism of action of HOTAIR in breast cancer development, researchers want to find out more accurate molecular targets that may guide to more customized treatment in breast cancer patients, particularly patients with metastasized or resistant to the conventional treatment of breast cancer (Mozdarani et al., 2020).

As morbidity and mortality rates of breast cancer are high, there is an immediate need to find more effective forms of treatments. The exploration of the molecular processes of drugs such as quinazoline derivatives and other responsible factors such as HOTAIR may lead to the introduction of tailored therapies that would supersede the current shortfalls of the available treatment strategies by enhancing the chances of survival in breast cancer patients (Salah Eldeen et al., 2025). The identified HOTAIR as a structurally intricate, regulation lncRNA, which is inactive as an enzyme, which complicates and renders HOTAIR a non-conventional and challenging drug target. The novelty of the use of small-molecule quinazoline derivatives to regulate the structure and function of HOTAIR and complemented by RNA-focused docking, dynamics simulations and experimental cytotoxicity data. This combined approach places the research in the new paradigm of RNA-targeted therapeutics and explains well the novelty and translational issues of lncRNA drug discovery.

The hypothesis is that these derivatives are capable of interfering with the scaffolding activities of HOTAIR that will prevent the proliferation of cancer cells. The study design will be used to test this by first the 25 compounds are screened by the initial molecular dock and subsequently 100-nanosecond molecular dynamics is used to validate the structural stability of the P14-HOTAIR complex. These in silico results are then compared to biological information of MTT cytotoxicity assays on the MCF-7 cell lines to find the $IC_{50}$ values and general anti-proliferative activities. The primary objective of this study is the computational identification and virtual screening of quinazoline derivatives targeting HOTAIR, while experimental cytotoxicity evaluation serves as secondary biological validation of the computational predictions.

To begin with, the RNA architecture of HOTAIR on which docking occurred was computationally determined because experimental high-resolution structures have not been determined yet, and this could have an effect on the accuracy of the binding. Second, computational predictions (docking, MD, ADMET) give positive but not conclusive biological data and need additional confirmation. Third, it only tested in vitro cytotoxicity in a single cell line in breast cancer cells (MCF-7) not against normal cell controls or the standard anticancer drugs. Lastly, solubility and toxicity (as well as other concerns in the ADMET liabilities) predicted, suggest optimization and thorough in vivo pharmacokinetic and safety investigations prior to translational progression.

To strengthen the scientific rationale for directly targeting the long non-coding RNA HOTAIR using small-molecule modulators by integrating evidence from prior studies on RNA draggability (Zamani and Suzuki, 2021; Zhao et al., 2022). The study aims to contextualize HOTAIR within the expanding paradigm of RNA-targeted therapeutics, highlighting precedents where structured RNAs have been successfully engaged by small molecules with high affinity and selectivity. Additionally, this work seeks to synthesize mechanistic insights from established RNA-ligand interactions to justify the feasibility of pharmacologically modulating HOTAIR structure and function. Importantly, structured RNAs have demonstrated small-molecule binding capacity with therapeutically relevant affinity, supporting the feasibility of pharmacologically modulating HOTAIR through targeted quinazoline derivatives.

Recent advances in RNA-targeted drug discovery have demonstrated that small molecules can selectively bind structured RNA motifs with nanomolar affinity, as exemplified by risdiplam targeting SMN2 pre-mRNA and branaplam modulating RNA splicing. These clinically validated precedents confirm that structured non-coding RNAs represent viable pharmacological targets and support the rationale for targeting HOTAIR, which possesses structurally defined domains amenable to small-molecule engagement. The expanding RNA druggability landscape reinforces the translational potential of this computational screening approach for identifying novel RNA-binding lead compounds.

The main aim of this paper is to critically review the therapeutic value of quinazoline analogues that act on the long non-coding RNA HOTAIR in breast cancer. Particularly, the paper will (i) clarify molecular mechanisms of quinazoline analogues and HOTAIR interaction by computational chemistry, (ii) determine lead compounds, which have the highest binding affinity, stability and drug-like properties, (iii) confirm the anticancer activity through cytotoxicity analysis in vitro and (iv) determine pharmacokinetic and toxicity properties by ADMET assessment. The manuscript, further, attempts to combine both computational and experimental results to give a translational framework of how to develop the RNA-targeted quinazoline derivatives to preclinical development.

## 2. Materials and methods

### 2.1. Materials

The supplier of chemical reagents as well as solvents to be used in this study was Sigma Aldrich. The process that was used to monitor as well as record all the chemical reactions was the thin-layer chromatography (TLC). The preparation of the plastic sheets prior to usage included the application treatment to create a layer of silica gel of 0.2 mm having a bond with an indicator called E. Merck. Melting point was determined by means of a Stuart electrothermal melting point with stable readings. Infrared spectra analysis was done using KBr disc, which was made in the Bruker spectrophotometer available in Mumbai India. In the city of Mumbai, India, NMR spectra of 1 H as well as 13 C were taken in Bruker magnet of 400 MHZ frequency. The instrument that was used to collect mass spectrometry data was the Shimadzu GC MS QP 5000 quadrupole mass spectrometer at Chennai, India. The internal standard employed was TMS and chemical shifts were performed in terms of parts per million (ppm). DMSO-d6 or CDCl3 was used as a solvent system by the researchers. The equipment used in the present study VARIO- Elementer was used to identify the elements in samples collected in Mumbai, India, which included carbon (C), hydrogen (H) and nitrogen (N).

## 2.2. Computational sections

### 2.2.1. Network analysis

RNA interaction networks developed by the STRING database assisted the researchers in identifying the primary RNA that were pertinent to cancer most importantly those RNA that dealt with breast cancer. The process determines vital proteins through visualization of their functional bond design. The study employed Graph Theory and both degree centrality and betweenness centrality and clustering coefficients were calculated in order to identify leading RNA of network topology. To study the biochemical pathways and signaling process involved in breast cancer progression, KEGG database was used. The comprehensive analysis of molecular targets via this method enhances information in regard to development of new medical strategies via therapies on the targets (Kunjiappan et al., 2020a, 2020b; Li et al., 2020).

### 2.2.2. RNA structure preparation

The structural prediction with the most reliable three-dimensional structural model of the target could be achieved with only the 5 domain (of about 300 nucleotides) of (HOX transcript antisense intergenic RNA) HOTAIR. The major sequence of this certain area of HOTAIR was carefully copied out of the National Center of Biotechnology Information, (NCBI) database. Then, the three-dimensional framework of this domain in RNA was forecasted by applying a universal and specific synthetic device called RNA Composer. Through the most powerful algorithms and the vast knowledge database of secondary and tertiary RNA structures, RNA Composer is able to create high-fidelity structural model that is necessary in further molecular simulation work. This type of homology modelling was essential due to the fact that at present there are still no high-resolution experimental structures of the full-length HOTAIR RNA. This domain was selected based on its established functional relevance in mediating PRC2 and LSD1 recruitment, which are central to HOTAIR-driven epigenetic silencing of tumor suppressor genes. The structural model generated by RNA Composer was assessed for fold quality and secondary structure consistency, though it is acknowledged that computational prediction introduces inherent limitations in binding accuracy compared to experimentally determined high-resolution structures.

Special types of computational tools were applied to the analysis pipeline in order to resolve the peculiarities of RNA structure and identify druggable pockets. Selective, small molecules that target RNA are of interest in modulating RNA, controlling gene expression and potentially diversifying the field of therapeutic targets away from RNA-based targets. Nevertheless, it is not yet possible to identify RNA binding sites capable of accepting ligands with a drug-like physicochemical profile. To mitigate this, a strong and free tool (*fpocketr*) was utilized in identifying, characterizing and displaying the possible binding sites of the ligands on the surface of the HOTAIR RNA. Aimed at being optimized by a deep search to known RNA-ligand complexes, *fpocketr* allowed identifying structurally relevant and chemically accessible pockets with the prospect of being approached by small molecules in a productive manner. This tool was critical in speeding up the discovery of druggable sites at the early-stage which formed a cornerstone in the rational development of RNA-based therapeutics.

The selection of the 5′ domain of HOTAIR for molecular docking was specifically guided by its critical role as the PRC2-binding module responsible for chromatin remodeling and transcriptional silencing. This domain contains structurally conserved secondary structure elements including stem-loops and internal loops that create well-defined binding pockets suitable for small-molecule targeting, as confirmed by the fpocketr pocket detection analysis. The biological significance of this domain in HOTAIR-mediated oncogenic function makes it the most rational target for computational drug screening.

### 2.2.3. Ligand preparation

The HOTAIR was employed to produce the docking results of the analysis of the compound with various cocrystal line variations (P1–25). The files of the necessary format. sdp were found in the PubChem database that was available at https://pubchem.ncbi.nlm.nih.gov/. Analysis of the designed cocrystals was done along with the compounds in bio-visualization tool software BIOVIA Discovery studio Visualizer (Kalimuthu et al., 2022).

Molecular docking was done based on the 3D template of the HOTAIR domain to obtain potential lead compounds using the predicted structure of the domain. The method is a critical computational method which has made possible the efficient screening of a chemically wide range of library of small molecules that have attractive binding interactions with the RNA target. Docking methods had to be tuned well to take into consideration the structural and electrostatic nature of the interactions between RNA and its binding ligand, as well as the precise determination of binding modes and initial affinity orders. As an aim to simplify the recognition of bioactive compounds with possible therapeutic significance, which is of great significance to both chemical biology and drug discovery, the open-source docking tool was utilized; The platform was able to offer a solid basis to assess molecular interactions and make fever candidates available to be tested in the laboratory.

### 2.2.4. Molecular docking protocol

The RNA and ligands were treated and converted into pdbqt file formats with the use of AutoDock Vina-POAP software to conduct virtual screening activities. In the setup file, it had the data regarding the RNA along with ligands and information regarding the grid box parameters. AutoDock Vina-POAP processes produced polar hydrogen, solvation, and fragmental volume conditions in the course of conducting a digital screening on the RNA. AutoGrid also developed the grid box of the grid map, which was the x (43.18), y (18.13), and z (81.27) points of map coordinates intersection. The calculation process could be done faster due to the existence of the score grid that was a reflection of the ligand structure. The local search global optimization algorithm that gets executed by AutoDock Vina has a series of iterations and binds the RNA and ligands by keeping them with their pre-determined structure. Binding free energy output was provided in the experiment and only qualified under large positional root mean square deviation exclusion filter exceeding 1.0Angstrom. The RNA interaction measurement was done based on the highest binding affinity, which included the lowest binding site as the measurement criterion used by BIOVIA Discovery Studio Visualizer (Palanichamy et al., 2022; Panneerselvam et al., 2022; Jiang et al., 2024). The docking protocol was validated through pose reproducibility assessment and binding energy ranking consistency. Selection of the best docking pose was based on the lowest binding energy criterion combined with RMSD exclusion filters, ensuring reliability of the reported docking scores.

Furthermore, grid box dimensions were centered on the identified druggable pocket with coordinates $x = 43.18$, $y = 18.13$, $z = 81.27$, and exhaustiveness parameters ensured adequate conformational sampling. Top-scoring poses were evaluated for chemical reasonableness of binding interactions, and only poses demonstrating consistent hydrogen bonding patterns with key nucleotide residues were retained for downstream molecular dynamics validation.

### 2.2.5. Molecular dynamics simulation

Stability and variability patterns in RNA-ligand complexes have been assessed by the researchers as the key goal of these MD simulations. The principal aim was to infer the way in which therapeutic compounds bind to target RNA. The simulations were done on Linux system using Desmond module under Schrodinger and maestro interface to carry out simulation control. The HOTAIR RNA-P14 complex (RNA + ligand) was simulated in the box of solvents, explicitly in the presence of TIP3P water, through the OPLS-4 force field. The net charge of the RNA system was neutralised by adding counterions; further $Na^+/Cl^-$ ions were added so that the end ionic strength was 0.15 M NaCl. The last system was hence made up of RNA, ligand, water molecules, and neutralising/ physiological ions. This explanation has been incorporated so that there can be transparency and reproducibility of the MD set up. Data analysis carried out in the simulation was carefully examined by Desmond module of Schrodinger. The parameters of stability were determined by the researchers using simulation interaction diagrams to which they calculated the ligand-RNA complex. A research group assessed values of RMSD and RMSF and examined RNA-ligand interactions during the simulation over 100 nanoseconds (Rajeshkumar et al., 2022; Saravanan et al., 2019). The equilibration protocol consisted of initial energy minimization followed by restrained equilibration under NVT and NPT ensembles before the 100 ns production run at 300 K and 1 atm pressure. Cutoff distances for non-bonded interactions were set at standard values, and the integration time step was maintained at 2 fs throughout the simulation.

The OPLS-4 force field was selected based on its validated performance in modeling biomolecular systems including nucleic acid-ligand complexes, providing accurate representation of non-bonded interactions critical for RNA-ligand binding studies. Trajectory frames were saved at 100 ps intervals for post-simulation analysis, and the protocol follows established best practices for RNA-ligand molecular dynamics studies.

### 2.2.6. *ADMET studies*

The ADME profiles were tested along with the physicochemical properties of compound P14 to determine their efficiency to perform with the help of calculational procedures (Mandhadi et al., 2020). Some of the parameters that were calculated using the SwissADME web tool were molecular weight, molar refractivity, solubility, bioavailability, radar map, brain penetration as well as the human gastrointestinal absorption that were calculated at (http://www.swissadme.ch/). SwissADME online service offers free services to researchers on the prediction of how experimental and reference compounds perform in the process of drug pharmacokinetics and drug-like behavior testing. SMARTCyp software offered an assessment of ligand metabolism by CYP450 system with the processing of SMILES code of P14.

### 2.2.7. *Density functionality theory*

The available publicly available P14.sdp files were used in the scientific research, which are available in the PubChem database. The files were brought into the Spartan14 program by scientists to optimize its energy (Saravanan et al., 2019). The characterizations of the HOMO and LUMO levels by Hatree energy were carried out on GaussView 6.0.16 software. The values of Hatree energies were also converted to the units of electron-volt to calculate the HOMO-LUMO energy gaps. The alteration of the HOMO-LUMO energy gaps assessment of a molecule plays a significant role in the chemical stability assessment of P14.

## 2.3. *Experimental sections*

### 2.3.1. *Step 1*

Central Composite Design (CCD) analysis was of great significance as far as the factors which determined the yield were concerned (Bhattacharya, 2021; Ruslan et al., 2021). The ANOVA of the quadratic model is statistically significant due to F-value of 7.21 and p-value of 0.0024. Non-linear effects seem to play a significant role in determining quadratic terms $A^2$, $B^2$ and $C^2$ with significant values which does contribute to determination of the yield. The single variables and also the interaction effects of A, B, and C were not seen to be statistically significant ($p > 0.05$) as quadratic effects had a bigger influence in the yield. The yield prediction model has $R^2$ of 0.8665, as a satisfactory value of the model that explains the 86.65 of yield variations. Though the adjusted $R^2$ (0.7463) has some signs of an overfit model, it gives a negative value of predicted $R^2$ (-0.0082), meaning that there is less accurate prediction of subsequent data values. The signal strength of navigating the design space also passes the test since the minimum value of adequate precision is 6.7746 above the range of target at 4. The last quadratic model reveals that temperature in conjunction with solvent and time is significant in production of yield due to the quadratic input. The low level of multicollinearity on the factors can be seen based on the high VIF estimations that are close to a value of 1. The prediction accuracy of model reduction could be better yet the quadratic model selected is most applicable to the data due to its significant factors being important and the adjusted $R^2$ high scores. Subsequent investigations ought to assist in the determination of the best factor parameters that are standard to enhance the results of the production Fig. 1.

### 2.3.2. *Step 2*

According to the analysis of variance (ANOVA), the quadratic set was found to be statistically significant with a value of F, 8.21 and p, 0.0014 and hence it is appropriate to be used to predict the responses. An F-value such as this could only appear randomly 0.14 % of the time. The terms C (Time) ($p = 0.0093$), $A^2$ (Temperature squared) ($p = 0.0004$), $B^2$ (Solvent squared) ($p = 0.0002$) and $C^2$ (Time squared) ($p = 0.0026$) came out as statistically significant. The quadratic terms also have substantial impacts on the level of yields substantiating the need of using second-order polynomial-based models. Based on the estimated coefficients coded variable for Time C had positive impact yet $A^2$, $B^2$ and $C^2$ had negative impact therefore indicating presence of nonlinearities. This is essentially true since most of the variance inflation factors (VIFs) are close to 1 implying that there is no multicollinearity between the terms in the model. The model worked well with the Adjusted $R^2$ at 0.7735 but there was a big difference between the Predicted $R^2$ which was 0.0959. The overview of such a shortfall in this model shows the potential population whose values are not within the general ranges of data points or those that need correction of their responses. The fit statistics reveal amounts of probability of the validity to be 6.781 which confirms that the model provides enough signal-to-noise resolution in order to explore the design space in an adequate way. The optimal absence of fit implies more work that should be done by the researchers on their model. It is possible to improve predictive accuracy and model robustness through either response transformation procedures and model reduction approaches or additional experimentation. The quadratic model is a valid tool of prediction because it explains better than an inconsistent model using linear and the two factorial interaction which are poor in the $R^2$ factor. Further confirmation runs in conjunction with the improvement procedures should be carried out to certify predictions and establish accurate process conditions to produce optimum outputs Fig. 2.

### 2.3.3. *Procedure*

#### 2.3.3.1. *Step1.*

In an ice bath cooling solution of N-cyclohexyl-2-phenylacetamide and benzonitrile (1-chloropyridine and 9:1 dichloromethane 1.7 mL) was allowed to react till 2 min of the trifluoromethanesulfonic anhydride started falling through the syringe. The mixture of N-cyclohexyl-2-phenylacetamide and benzonitrile in combination with 2-chloropyridine in dichloro-methane (1.7 mL) had to be stirred under the condition of an ice bathing (5 min) and after that it was kept at room temperature (5 min) and then it was brought into effect. This was put in a preheated oil bath at a temperature of 45 0 C and left to react 16 h. The precipitate had cooling to room temperature to give white solid 2-benzyl-4-phenyl-5,6,7,8-tetrahydroquinazoline 1I (86%).

#### 2.3.3.2. *Step2.*

2 mmol of Methyl-substituted quinazoline 1I was then dissolved in 8.5 mL of 96 ethanol and its expected single equivalent of

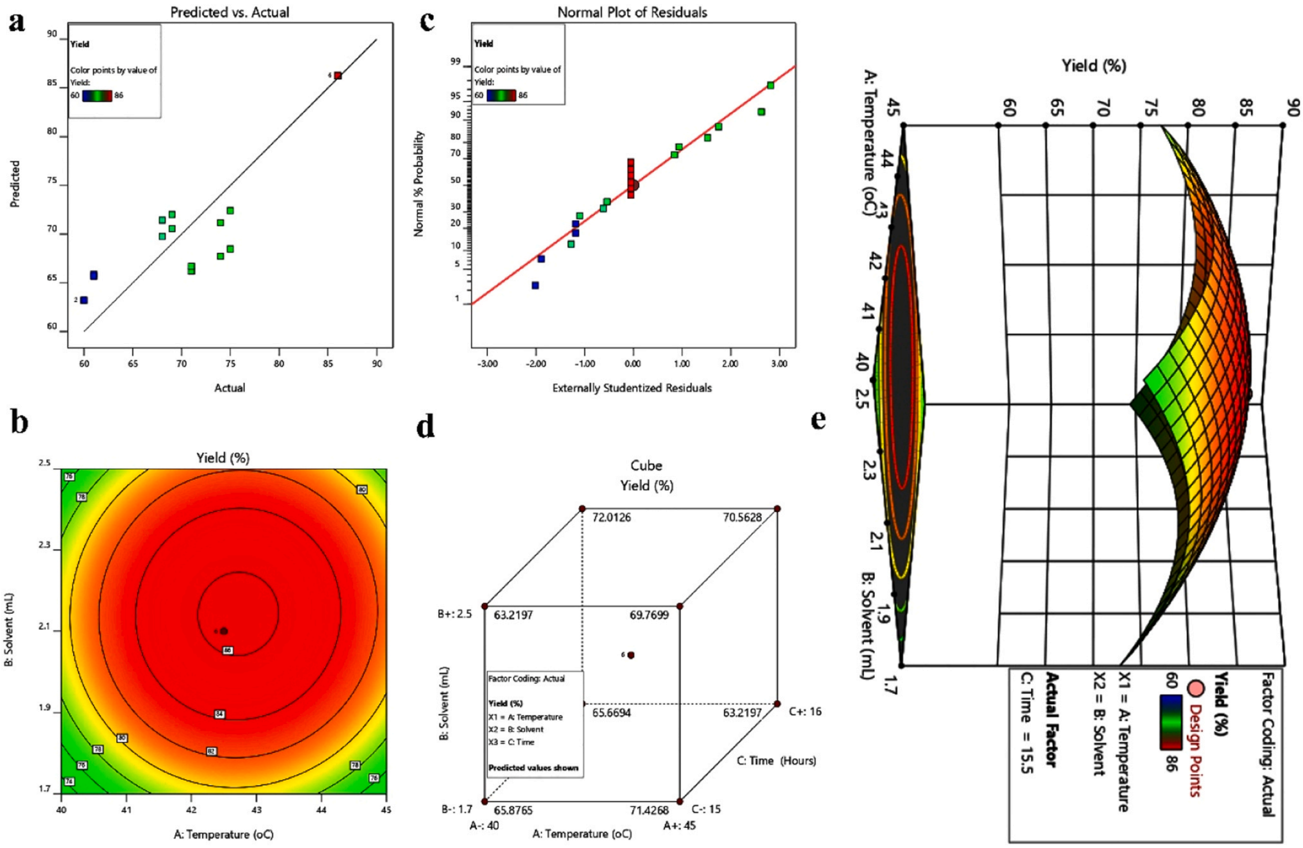

**Fig. 1.** Statistical and response surface analysis of step 1 yield (%). (a) Predicted vs. actual values, (b) Contour plot, (c) Normal probability plot, (d) Cube plot, and (e) 3D surface plot showing optimization trends.

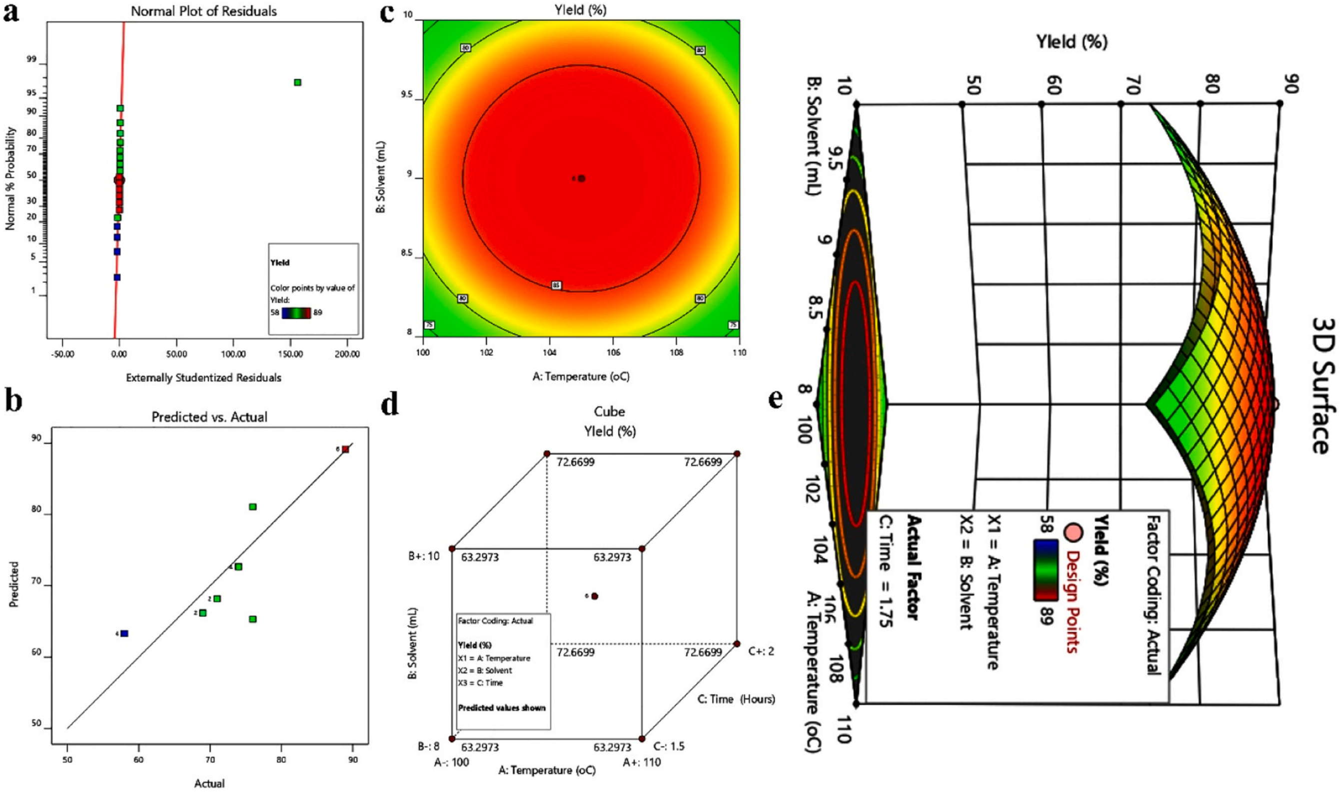

**Fig. 2.** Statistical and response surface analysis of step 2 yield (%). (a) Normal probability plot, (b) Predicted vs. actual values, (c) Contour plot, (d) Cube plot, and (e) 3D surface plot illustrating optimization trends.

substituted benzaldehyde was added under micropipette. At 110 oC, the mixture was stirred at 115 min, the mixture formed the product that was set at room temperature. The product then needed to be filtered whereby we used numerous steps of ethanol washings (total volume of 5 mL). The ethanol recrystallization involved boiling the product P1 and P10 and P13 and P19 followed by the drying process that gave 92 % of the final product Scheme 1

#### 2.3.4. *Formulation of SLNs-encapsulated 2-(2-(3-nitrophenyl)-1-phenylvinyl)-4-phenyl-5,6,7,8-tetrahydroquinazoline (P14)*

The preparation of three independent SLN batches in order to encapsulate P14 as a formulation method to enhance its delivery properties. Lipid matrix was utilised, which was Cetyl palmitate, and dissolved in an organic solvent and heated to obtain a homogeneous lipid phase. P14 was added to this lipid phase and ultrasonic was carried out to form a microemulsion with polysorbate-80 and sodium deoxycholate as stabilising surfactants. Isolation of the resulting SLNs was done by ultracentrifugation at 10, 000 rpm. The drug loading capacity and encapsulation efficiency were then determined with the help of standard equations. This method of formulation proves the viability of SLNs as a carrier system to increase the physicochemical and delivery capacity of P14. Specifically, the lipid phase consisted of cetyl palmitate dissolved in an organic solvent at elevated temperature, with P14 incorporated at a defined drug-to-lipid ratio. Ultrasonication was performed at controlled amplitude and duration settings, and the resulting emulsion was stabilized using polysorbate-80 and sodium deoxycholate as surfactants before ultracentrifugation isolation at 10,000 rpm.

#### 2.3.5. *In vitro drug release, kinetics, and stability studies of SLNs-encapsulated P14*

In vitro drug release of SLNs was determined by dialysis bag diffusion technique. In this procedure, SLNs were transferred in dialysis bags (molecular weight cut off 3500 Da) and incubated in release mediums adjusted at different pH values (acetate pH 4.4 and phosphate pH 7.2) at 37 °C. With the release of P14 loaded in the SLN, the release of P14 was determined by HPLC. For this method of administration, it was necessary to have complete information about the slow-release kinetics of the drug, in order to calculate the release profile of the drug and to ensure that the SLNs are able to deliver (long-term).

The in vitro release kinetics of the P14 from the SLNs were determined to understand the mechanism of release from the SLNs. The cumulative rate of drug release versus time was fitted to a range of mathematical models including Zero-order, First-order, Higuchi, Korsmeyer-Peppas and Hixson-Crowell models. The model with maximum coefficient of determination ($R^2$) value was considered as the best model. The release behaviour and the optimization of formulation with respect to the sustained release profile is essential for the understanding of the kinetic of the release mechanism and to maintain the long-lasting therapeutic effects of the *P14*.

Under different physiological conditions for the simulation of *in-vivo* condition, the stability of the P14-loaded SLNs was assessed. SLNs were incubated in NaCl, bovine serum albumin (BSA), acetate and phosphate buffer solutions at 35°C, pH 4.4 and pH 7.2. The structural stability of the SLNs was observed by UV–visible spectroscopy via time-dependent change in absorbance (λ max). Results of this analysis provided valuable information on the intactness of the SLNs and their ability to stabilize the encapsulated P14 under different physiological conditions. The results revealed that the SLNs do not lose their structural integrity and are able to retain the *P14* effectively for their future application.

#### 2.3.6. *LC-MS, FTIR and XRAY characterization of SLNs-encapsulated P14*

The stability and functionality of encapsulated P14-loaded SLNs were confirmed by Liquid Chromatography-Mass Spectrometry (LC-MS). This method was performed to determine the active compounds in the SLNs. The LC-MS results established good encapsulation, since no degradation and/or loss of the P14 was detected. The spectral data showed the stability of the encapsulated drug, thus proving that the P14 can be successfully incorporated into the SLN formulation and delivered without affecting its integrity.

Fourier Transform Infrared Spectroscopy (FTIR) was used to record the molecular interaction between P14 Loaded and the SLNs as well as the structural changes. IR spectra were recorded by Shimadzu IR Tracer-100 at 400–4000 $cm^{-1}$. This discussion has revealed functional groups involved in encapsulation process and provided information if there is any interaction of SEA loaded SLNs with lipid components of SLNs. FTIR analysis gave key information with great significance relating to compatibility of formulation and the formulation was found to be compatible at molecular level and *P14* loaded was not altered during encapsulation process.

The structural characterization of P14 was performed using X-ray diffraction analysis on a Bruker D8 Advance diffractometer equipped with Cu Kα radiation (λ = 1.5418 Å). The compound was prepared by grinding crystalline P14 into fine powder using an agate mortar and pestle. Approximately 50–100 mg of powdered P14 was uniformly packed into an aluminum sample holder, ensuring a flat surface to minimize preferred orientation effects. The XRD measurement was

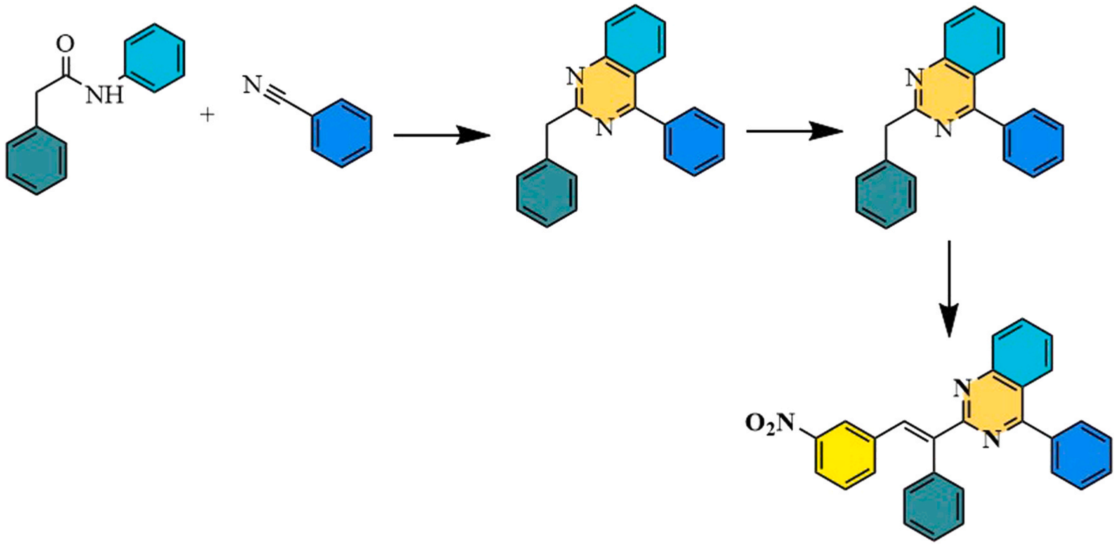

**Scheme 1.** Synthesis of 2-(2-(3-nitrophenyl)-1-phenylvinyl)-4-phenyl-5,6,7,8-tetrahydroquinazoline derivatives.

conducted at room temperature (25°C) with scanning parameters set at 40 kV voltage and 40 mA current. Data collection was performed over a 2θ range of 10–90° with a step size of 0.02° and counting time of 2 s per step. The obtained diffraction pattern was analyzed using MATCH! phase identification software and compared with the International Centre for Diffraction Data (ICDD) database. Peak indexing was performed using unit cell refinement algorithms to determine Miller indices for each reflection. The crystallite size was calculated using the Scherrer equation, and peak positions were calibrated against silicon standard to ensure accurate ᴅ-spacing calculations for structural correlation with the proposed molecular framework.

### 2.3.7. FE-SEM and particle size analysis of SLNs-encapsulated P14

The morphology of P14 Loaded-SLNs and the size distribution were examined by scanning electron microscopy (FE-SEM). The freeze-dried SLNs were further dried in distilled water and were taken. The FE-SEM showed the obvious images of the SLNs and confirms the homogeneity and stability of the SLNs. This method was also used to prove the compatibility of the SLNs as drug delivery vehicle and provided further reasons to support the potential use of the SLNs as controlled drug delivery system.

A series of procedure for characterization of *P14* loaded SLNs including determination of particle size, size distribution, surface charge, and colloidal stability are examined. As the first step, the particle size and size distribution are measured by dynamic light scattering (DLS). For drug delivery applications, particle size should be in the range between 180 and 200 nm with narrow and monomodal distribution. The volume distribution is examined to confirm that particles are in the range of 150–250 nm with a peak intensity of 35%. This confirms that the SLNs are homogeneously formed particles with batch consistency and reproducibility. Zeta potential measurements are performed with the aim of characterizing the surface charge of the nanoparticles. Maximum Zeta Potential equal to −25 mV, values from −15 to −35 mV This negative surface charge represents electrostatic stabilization, such that aggregation is avoided by electrostatic repulsion forces. Zeta potential values of above + /- 20 mV are considered to be acceptable for colloidal stability and potential for long-term storage and resistance to flocculation. Stability of the formulation is determined by particle size stability and Zeta potential stability over time. The results indicate that the *P14*-loaded SLNs have the desired physicochemical properties such as optimum particle size, narrow distribution, stable surface charge to achieve satisfactory formulation for drug delivery system.

### 2.3.8. MTT assay

The MCF-7 human breast adenocarcinoma cells were purchased based on an authenticated national cell repository, and cultured in accordance with supplier specifications, and mycoplasma status was regularly determined. A specified range of concentrations of P14 (e.g. 6.25, 12.5, 25, 50 and 100 µg/mL per well) was used in the experiments of cytotoxicity. Triplicate testing was done on each condition and at least three separate experiments done. Nonlinear dose-response curves were then used to estimate the $IC_{50}$ values using a respective curve-fitting software and the analysis comparisons between groups were done using standard statistical tests (mean +- SD), which are now appropriately mentioned in the revised manuscript. In their incubator, the MCF-7 cells they grew under the conditions of 37 °C 5 % $CO_2$ and 100 IU/mL penicillin and 100 g/mL of streptomycin in DMEM media with 10 % deactivated Fetal Bovine Serum (FBS). It was through the procedure of trypsinization of monolayer cells that it became possible to arrive at 1.0 × 105 cells/mL concentration of the medium solution at a medium solution of 10 % FBS. Cell suspension of 1 × 104 cells was added to the plated wells in 100 µL of volume. When a partially confluent layer was obtained the researchers removed the culture medium and then washed the cells once with medium. The chosen well concentrations were incubated with the test solutions of 100 µL volume at 37 °C in the incubation conditions of 5% $CO_2$ with another 24-h incubation. The solutions obtained in the experiment were then replaced by 20 µL of MTT solution (2 mg/mL MTT in PBS) which was added to each well. The testing plate was incubated after four hours at the specific temperature conditions of $CO_2$ atmosphere. The supernatant fluid was collected by the researcher after incubation and 100 µL of DMSO was added. To resolve the formed formazan the operator has added gentle agitation moving through the plate. Cell viability was determined by microplate reader at 570 nm of wavelength. The formula that was used to determine viability percentage is % viability = (Sample abs/Control abs x 100). Each concentration was tested in triplicate wells per plate, and at least three independent biological experiments (n = 3) were conducted. $IC_{50}$ values were estimated using nonlinear regression dose-response curve fitting. Results are expressed as mean ± standard deviation, and coefficient of variation was calculated to assess intergroup variability. It is acknowledged that 95% confidence intervals for $IC_{50}$ values and formal statistical significance testing with p-values will be essential components of future comprehensive pharmacological evaluations.

To enhance statistical rigor in future comprehensive evaluations, one-way ANOVA with Tukey post-hoc comparison will be employed for multi-group cytotoxicity analysis. Additionally, 95% confidence intervals will be reported for all $IC_{50}$ determinations, appropriate positive controls using established anticancer agents such as doxorubicin or cisplatin will be included for benchmarking, and selectivity indices will be calculated by comparing $IC_{50}$ values against normal breast epithelial cell lines (MCF-10A) to establish the therapeutic window.

## 3. Results and discussion

### 3.1. Computational sections

### 3.1.1. Network pharmacology

The Gene Ontology (GO) enrichment analysis shows that the study is highly concentrated in processes concerning miRNA regulation as the strongest enrichment is associated with the process of regulating the miRNA metabolism processes and transcription. The biological processes were characterized by large signal values and very low false discovery rates (FDR) signifying strong associations. As seen in the network visualization (panel b), a wide range of different genes such as MYC, MDM2, and POLR2A are well-clustered together, which is indicative of a possible cooperation in miRNA regulation. Dominant location of the important transcription factors (e.g., POLR2A, MDM2) points out to the key roles of the same elements of regulation in the cellular context, hence the importance in the RNA metabolism and transcriptional regulation. The most significant 30 genes in this study were analyzed in relation to diverse network measures, in order to determine their structural significance and any possible role in any cellular processes. The outcomes showed that HOTAIR, having an indegree of 66, had the greatest betweenness of 281.241 an indication that it plays a very critical role in the connectivity of different parts of the network. Likewise, MYC showed a high degree of centrality in networks (64) which revealed its ability to be considered as a regulatory core of gene. The proximity scores of both HOTAIR and MYC (0.01064 and 0.01042 respectively) were similar indicating that both the genes were of similar proximity to the rest of the genes in the network. But they always had the eccentricity values of 0.5, and this can be a clue to uniformity of the connections within the network. The other genes with a betweenness significant of 63 (both) were ESR1 and EZH2. This implies that such genes could have critical functions of mediating the relationship between different signaling pathways. TP53, the parameter with the degree 61 showed a slightly lesser betweenness of 148.415, which may be concerning its secondary though still important contribution to the network structural integrity. It is also important to note that the radiality of these genes slightly varied, their scores being higher (2.825 and 2.8) which possibly suggests the impact they may have on the global network structure. HOTAIR, MYC and EZH2 exhibited the highest values of stress, which is a measure of network instability, therefore, these genes are strongly influenced by the network. It is interesting that genes which have smaller stress values, like PARP1 and EGFR may indicate that they could be less important in the network stability. All these findings help to confirm the possibility of the important role of the gene with a higher betweenness index and centrality index, like HOTAIR and MYC, will essentially play a hub in the molecular network that determines different cellular processes and disease mechanisms Table 1 and Fig. 3. Notably, these studies are not associated with such interaction between the quinazoline backbone and these genes. Rather, they put HOTAIR in perspective as a biologically relevant RNA target on which its regulatory network can be indirectly perturbed should small molecules, like quinazoline derivatives, effectively regulate the structure or activity of HOTAIR.

### 3.1.2. *Mechanism of action*

HOTAIR (HOX transcript antisense intergenic RNA) biological role has been massively confirmed by both clinical and molecular experiment results, making it one of the most vital epigenetic controllers and oncogenic drivers. The RT-qPCR and in situ hybridization studies have all indicated that it is overexpressed in various malignancies such as breast, colorectal, and liver cancer with high expression indicating poor patient survival and metastasis. It has been confirmed by mechanism validation that HOTAIR is a molecular scaffold and can recruit the PRC2 complex to cause H3K27 trimethylation and LSD1 complex to cause H3K4 demethylation that causes silencing of tumour-suppressor genes. Moreover, experiments using shRNA mediated knockdown in cell lines and xenograft mouse models demonstrate that HOTAIR depletion greatly decreases the cell proliferation and invasiveness, which makes it a feasible therapeutic target and a diagnostic biomarker in precision oncology. HOTAIR functions as a molecular scaffold, recruiting Polycomb Repressive Complex 2 (PRC2) and LSD1 histone-modifying complexes to target genes, leading to H3K27 trimethylation and transcriptional silencing of tumor suppressors. HOTAIR enhances breast cancer cell proliferation, invasion, and metastasis by regulating epithelial-mesenchymal transition (EMT). It modulates various signaling pathways including Wnt/β-catenin and PI3K/AKT. HOTAIR also acts as a competing endogenous RNA (ceRNA), sponging microRNAs like miR-7 and miR-34a, thereby upregulating oncogenes Fig. 4. Elevated HOTAIR expression correlates with poor prognosis, increased metastasis, and therapeutic resistance in breast cancer patients (Hussain et al., 2024; Zhou et al., 2021).

### 3.1.3. *Molecular docking analysis*

*3.1.3.1. Molecular docking analysis of HOTAIR-P1-25 complex.* To determine the binding affinity of 25 designed ligands to the target RNA, molecular docking analysis was undertaken. The docking scores quantifying the binding energy in kcal/mol were between −9.4 and −7.4, thus demonstrating moderate to strong interactions. P14 had the best binding affinity whose docking score was −9.4 kcal/mol implying that the likely binding process with the target RNA binds strongly and stably with the active site of the target RNA. P9 and P8 followed closely at −9.0 and −8.9 kcal/mol docking scores respectively illustrating their potential as lead compounds worth pursuing. P21, P6 and P25 also showed good binding energy (all $< -8.5$ kcal/mol), which suggests strong interaction, which should be investigated. Conversely, ligands such as P20, P18, and P23 exhibited lower binding affinities (32) (greater than or equal to −7.5 kcal/mol), indicating lighter interactions and relative smaller possible activity of target inhibition. All in all, the findings

**Table 1**
Network analysis of top 30 genes, showing their degree, betweenness, closeness, eccentricity, eigenvector, radiality, and stress values, highlighting their structural importance and potential roles within the cellular network.

| Name | Degree | Betweenness | Closeness | Eccentricity | EigenVector | Radiality | Stress |
|---|---|---|---|---|---|---|---|
| **HOTAIR** | 66 | 281.241 | 0.01064 | 0.5 | 0.17613 | 2.825 | 2574 |
| **MYC** | 64 | 218.969 | 0.01042 | 0.5 | 0.17483 | 2.8 | 2366 |
| **ESR1** | 63 | 189.689 | 0.01031 | 0.5 | 0.17345 | 2.7875 | 2158 |
| **EZH2** | 63 | 277.158 | 0.01031 | 0.5 | 0.16854 | 2.7875 | 2346 |
| **TP53** | 61 | 148.415 | 0.0101 | 0.5 | 0.17217 | 2.7625 | 1920 |
| **CTNNB1** | 56 | 115.67 | 0.00962 | 0.5 | 0.1612 | 2.7 | 1422 |
| **BRCA1** | 55 | 124.564 | 0.00952 | 0.5 | 0.15542 | 2.6875 | 1470 |
| **HDAC1** | 53 | 56.7966 | 0.00935 | 0.5 | 0.16168 | 2.6625 | 1014 |
| **ATM** | 53 | 132.074 | 0.00935 | 0.5 | 0.14889 | 2.6625 | 1394 |
| **CREBBP** | 53 | 79.2838 | 0.00935 | 0.5 | 0.1571 | 2.6625 | 1238 |
| **STAT3** | 50 | 76.0943 | 0.00909 | 0.5 | 0.15219 | 2.625 | 926 |
| **JUN** | 50 | 42.7056 | 0.00901 | 0.33333 | 0.15387 | 2.6125 | 766 |
| **AGO2** | 49 | 218.969 | 0.00901 | 0.5 | 0.12226 | 2.6125 | 1838 |
| **CREB1** | 49 | 50.2098 | 0.00901 | 0.5 | 0.15142 | 2.6125 | 852 |
| **TBP** | 48 | 123.091 | 0.00893 | 0.5 | 0.12831 | 2.6 | 1294 |
| **BCL2** | 47 | 32.201 | 0.00885 | 0.5 | 0.14922 | 2.5875 | 706 |
| **FOS** | 47 | 39.1452 | 0.00885 | 0.5 | 0.14572 | 2.5875 | 784 |
| **CDKN1A** | 46 | 37.131 | 0.00877 | 0.5 | 0.14641 | 2.575 | 592 |
| **HIF1A** | 46 | 30.935 | 0.00877 | 0.5 | 0.14654 | 2.575 | 588 |
| **AR** | 45 | 25.0794 | 0.0087 | 0.5 | 0.14441 | 2.5625 | 536 |
| **SMAD4** | 45 | 27.031 | 0.0087 | 0.5 | 0.14413 | 2.5625 | 564 |
| **SP1** | 45 | 56.1273 | 0.00862 | 0.33333 | 0.13719 | 2.55 | 728 |
| **CDK9** | 45 | 120.519 | 0.0087 | 0.5 | 0.11441 | 2.5625 | 1388 |
| **E2F1** | 45 | 24.1492 | 0.0087 | 0.5 | 0.14476 | 2.5625 | 520 |
| **RUNX1** | 44 | 30.6762 | 0.00855 | 0.33333 | 0.13935 | 2.5375 | 546 |
| **PTEN** | 44 | 28.9015 | 0.00862 | 0.5 | 0.14107 | 2.55 | 516 |
| **RELA** | 44 | 28.9062 | 0.00862 | 0.5 | 0.14111 | 2.55 | 508 |
| **TNF** | 44 | 22.4471 | 0.00862 | 0.5 | 0.14258 | 2.55 | 488 |
| **MDM2** | 43 | 16.5053 | 0.00855 | 0.5 | 0.1415 | 2.5375 | 380 |
| **STAT1** | 43 | 25.9695 | 0.00847 | 0.33333 | 0.13947 | 2.525 | 422 |
| **EGFR** | 42 | 15.1165 | 0.00847 | 0.5 | 0.13749 | 2.525 | 350 |
| **YY1** | 42 | 35.2119 | 0.00847 | 0.5 | 0.12852 | 2.525 | 630 |
| **DICER1** | 40 | 57.552 | 0.00833 | 0.5 | 0.11711 | 2.5 | 646 |
| **PARP1** | 40 | 14.4434 | 0.00833 | 0.5 | 0.13189 | 2.5 | 326 |
| **IL6** | 40 | 14.0578 | 0.00826 | 0.33333 | 0.1337 | 2.4875 | 272 |
| **DNMT1** | 40 | 23.9165 | 0.00826 | 0.33333 | 0.13103 | 2.4875 | 320 |

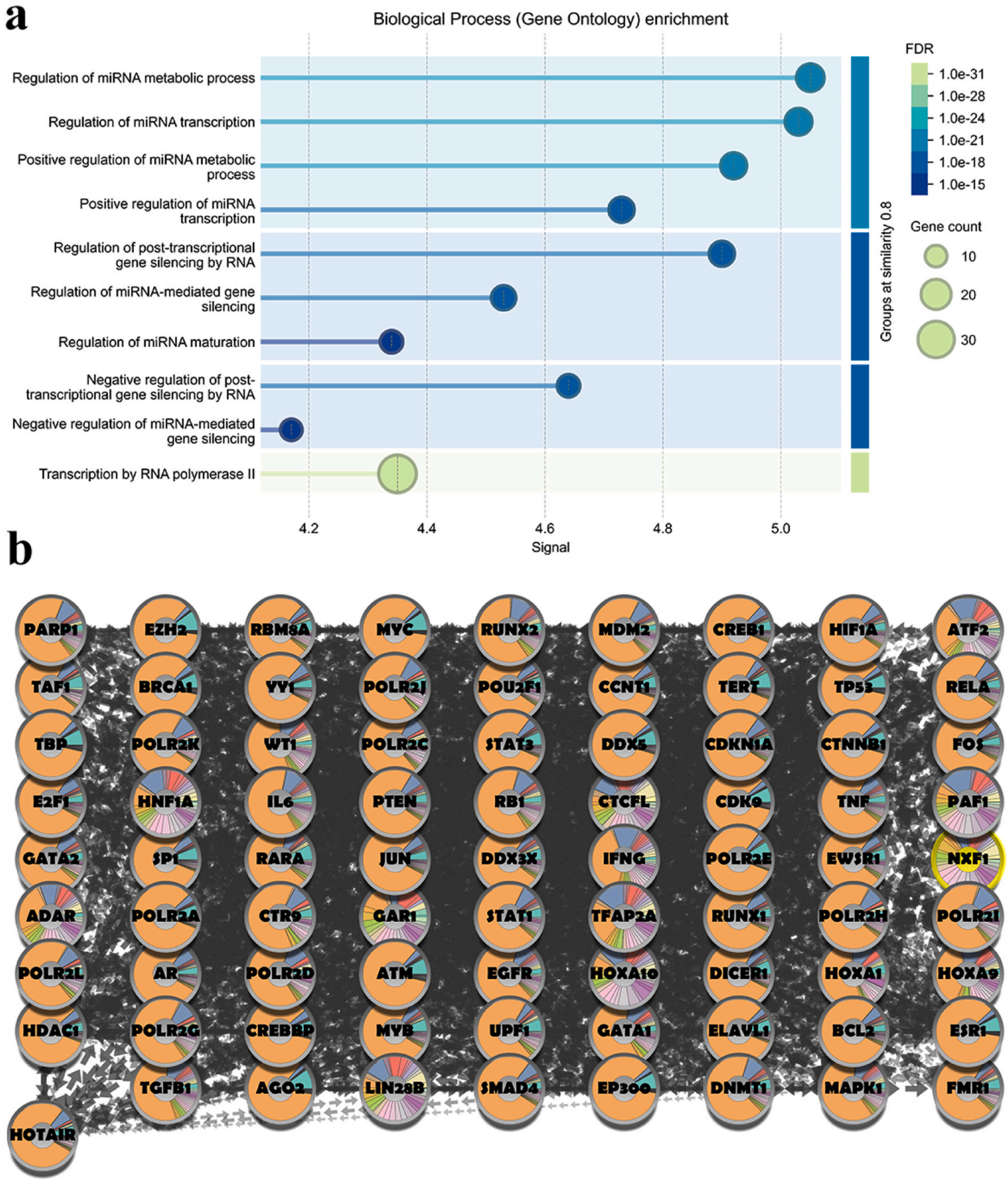

**Fig. 3.** Gene ontology enrichment and interaction network highlighting HOTAIR-centered regulation of miRNA processing, transcription, and oncogenic signaling pathways.

indicate that some of the ligands, especially P14, P9 and P8, have stronger binding potential. The above compounds must be ranked with regard to in vitro re-testing to understand their efficacy to refine them into potent therapeutic candidates.

*3.1.3.2. Molecular docking analysis of HOTAIR-P14 complex.* Molecular docking simulation of the small-molecule ligand to HOX Transcript Antisense RNA (HOTAIR) was carried out carefully to assess the binding strength and profile as well as the accommodation within the RNA school. The Fig. (5**a)** shows the image of the surface of the HOTAIR-ligand complex, which shows a complex of the active binding which is continually surrounding the ligand. The docking score achieved by the compound was −9.4 kcal/mol, which means that a compound had high binding affinity, which is a factor comparable to stable ligand-RNA interactions. The engulfing resides in the binding site created a specific hydrophobic cavity that further promoted the fitting of ligand by 1–1 arrangement and van der Waals pressure. As Fig. (5**b)** indicates, at the docking site, the zoomed image indicates that there are crucial interactions between the ligand object (represented in green stick model) and important nucleotides of the HOTAIR molecule. Hydrogen bonding of the ligand to U52 and A55 was established and stacking was also detected with G47 and G53 that contributes to the stability of conformation of the complex. Such interactions point towards the potential of the ligand to superimpose within a groove on HOTAIR that may disturb its secondary structure or activity. Fig. (5**c)** shows the complete-length model of the HOTAIR RNA with the docked ligand on the central positions in the helical backbone. The visualization ascertains that the ligand is located in a clearly defined grove which may lead to the suggestion that the ligand has the potency to alter structural motifs critical to the

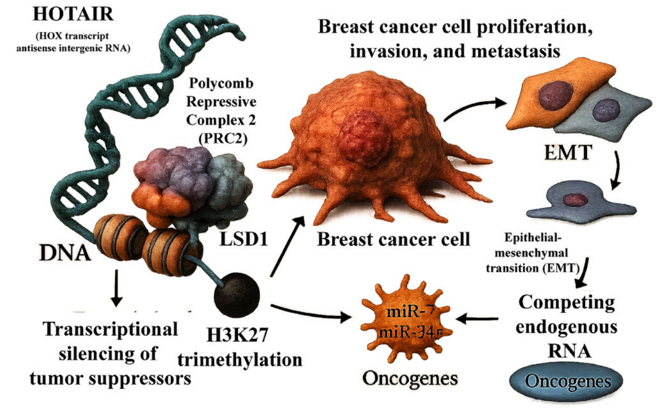

**Fig. 4.** Schematic illustration of HOTAIR-mediated epigenetic regulation driving EMT, oncogene activation, and breast cancer progression.

biological activity of HOTAIR. Notably, the positioning does not disrupt folding of the overall RNA structure suggesting specificity and low off-target influence of the structural disruption. The 3D interaction profile in (**5d**) also confirms the docking results as the ligand is seen to maintain positive binding interactions in the minor groove of HOTAIR. The relationship of molecular framework of the ligand is stabilized by electrostatic forces and network of hydrogen bonding through residues like C56 and G49. These results confirm that the ligand is optimally adapted to be accommodated in the RNA scaffold without causing conformational collapse to occur. All results concerning docking led towards the hypothesis that the chosen ligand has high binding capability towards the HOTAIR transcript. The way it binds sensitive areas of the RNA and the character of the molecule interactions indicates it may be a form of regulation and that this may be relevant in the treatment of its dysregulation associated diseases like various manifestations of cancer. Additional in vitro validation with respect to confirming inhibitory or modulatory properties of the ligand on the HOTAIR functioning would be justified. The resulting information on the involvement of the molecular interactions in the HOTAIR binding affinity and specificity as identified by the docking simulation and structural analysis of the HOTAIR-P14 complex was beneficial to appreciate the role played by the molecular interactions. As can be understood schematically in the 2D interaction map compiled in Fig. (6**a)**, there is a defined pattern of the inter-molecular contacts between P14 and the nucleotide bases of HOTAIR. As demonstrated by the magenta arrows, the ligand establishes multiple hydrogen bonds with some important nucleotides like G85, G86 and G88. The interaction of this hydrogen bond especially done by the hydroxyl (-OH) and amino (-NH) functional groups locks the ligand into one of the major grooves of RNA helix and thus a powerful and specific binding mode was promoted. Also, the interaction of the aliphatic rings of P14 and surrounding nucleobases is hydrophobic, and strengthens the complex. Fig. (6**b)** shows high-resolution 3D structure of the HOTAIR-P14 complex in showing the spatial orientation of P14 to the RNA architecture. The model of the yellow ribbon model depicts the RNA backbone, in which the molecule of P14 is observed fitting tightly into a helical cleft, where many non-covalent interactions have been formed. The pattern of binding of the ligand species within the groove of the RNA backbone, they are directly positioned in parallel to the helical axis, a configuration that could conceivably interfere with local secondary structure bases, or affect the dynamics of the RNA in its functional mode. The spatial position of P14 to structurally invariant nucleotides like G247, A248 and G249 give the indication that P14 may be involved in inhibition of the native folding pattern or checking the recognition elements necessary in RNA interactions. Hydrogen bonding together with hydrophobic stacking and spatial complementarity suggests P14 might be one of the compounds that prevents the structural and functional integrity of HOTAIR. The findings are relevant, taking into account the described epigenetic regulatory part of HOTAIR and its faulty expression linked with a number of malignancies. This can restrain the interactivity of P14 with chromatin-modifying complexes, like PRC2, which limits its oncogenic capabilities, regarding that the find interactivity of HOTAIR with this complex requires a binding to the functional region of HOTAIR that is stable. In summary, combination of the molecular docking and structural analysis of the HOTAIR-P14

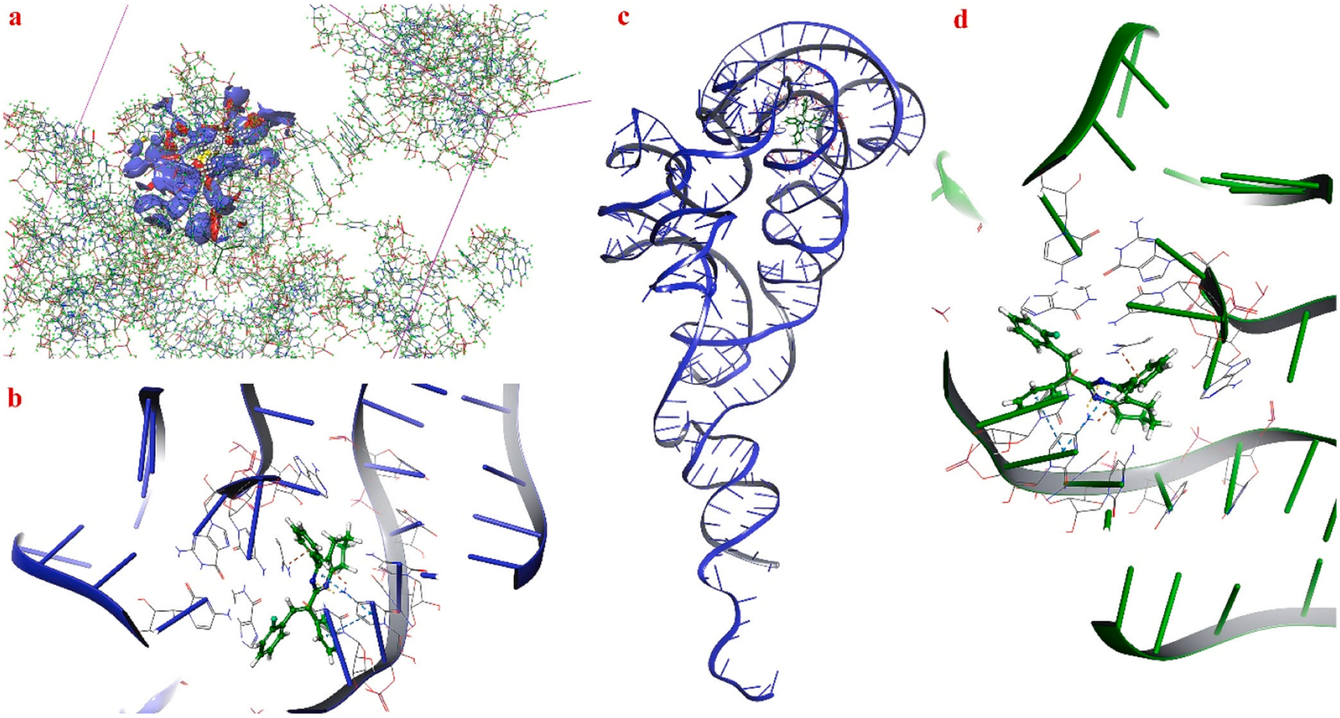

**Fig. 5.** Molecular docking visualization of compound–RNA complex highlighting binding within the HOTAIR pocket. Key nucleotide interactions with hydrogen bonding and stabilization patterns.

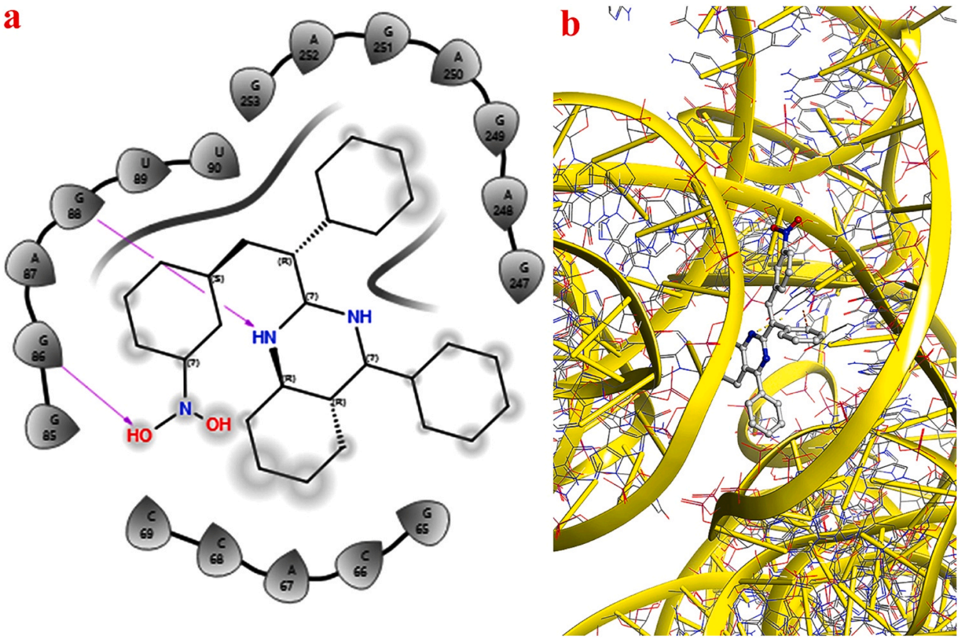

Fig. 6. Interaction diagram and three-dimensional docking pose of P14 within the HOTAIR RNA binding pocket, highlighting specific nucleotide contacts including G47, U52, G53, A55, G85, G86, and G88 with hydrogen-bond interactions.

complex supports an excellent binding footprint of P14, that has the ability to alter the biological output of HOTAIR or potentially block it. These findings provide a basis to perform further experiments with the aim of validating and developing P14 or its analogs as leads of therapeutic agents against HOTAIR-related pathologies Table 2.

**Table 2**
Integrated summary of docking affinity, molecular dynamics stability, ADMET characteristics, and in vitro cytotoxicity of lead compound P14, highlighting its HOTAIR-binding potential and therapeutic relevance in breast cancer.

| Parameter Category | Key Metrics | Observed Values (P14) | Interpretation / Relevance |
|---|---|---|---|
| **Molecular Docking** | Docking score (kcal/mol) | −9.4 | Strong binding affinity toward HOTAIR RNA |
| | Key interactions | H-bonds, π–π stacking with nucleotides | Stable and specific RNA–ligand binding |
| **Molecular Dynamics (100 ns)** | RMSD (Å) | 1.04–1.05 | High structural stability of HOTAIR–P14 complex |
| | RMSF (Å) | < 2.0 (core ligand atoms) | Limited atomic fluctuations |
| | Radius of gyration (Å) | ~20.6 | Maintained compactness |
| | SASA (Å$^2$) | ~714 | Stable solvent exposure |
| **ADMET Properties** | Molecular weight (Da) | 429.15 | Acceptable for lead optimization |
| | LogP | 6.22 | High lipophilicity (solubility concern) |
| | TPSA (Å$^2$) | 68.92 | Moderate polarity |
| | Oral bioavailability | Moderate | Requires formulation optimization |
| | Toxicity alerts | Hepatotoxicity, CYP inhibition | Needs further safety evaluation |
| ***In vitro* Cytotoxicity** | Cell line | MCF-7 | Breast cancer model |
| | IC$_{50}$ (μg/mL) | 23.9 | Moderate anticancer activity |
| | Response pattern | Dose-dependent | Consistent cytotoxic effect |

### 3.1.4. *Molecular dynamics analysis*

*3.1.4.1. Molecular dynamics analysis of HOTAIR-P14 complex.* To understand how stable and how the HOTAIR-P14 complex interacts MD simulation was done on complex at 100 ns simulation. The simulation analysis provides the insight into the nature of the complex in the dynamic environment paying special attention to the parameters of interest, which vary as follows: root-mean-square deviation (RMSD), root-mean-square fluctuation (RMSF), radius of gyration (Rg), solvent accessible surface area (SASA), and torsional angles distribution. Fig. (7**a)** displays typical shape of the HOTAIR-P14 complex that is characterized by the stable maintenance of the ligand in the RNA channel. The plot of Fig. (7**b)** is the illustration showing the time dependency of a number of structural quantities. The RMSD plot of the complex was mostly constant during the run with the average value of 1.04 A which indicated the structural convergence and approval of the conformational stability of the complex. The radius of gyration (Rg) also stayed at a similar value to around 20.6 A indicating the uniform compactness of the whole complex has been maintained through the simulation. The SASA analysis showed a constant value of around 714.05 Angstrom square which is an indication that there was very little variation in the exposure within the surface of the complex thereby confirming that there was stability in terms of solvation. Also, the potential energy curve had no extreme spikes, and it was smooth, which indicated that in the simulation, it will be thermodynamically stable. Fig. (7**c)** displays the distribution of the dihedral angles that are important to the ligand and its bound state structures in torsional angle space, and offers preferred conformational conformations in the ligand binding interaction. The Ramachandran-like plots of polar comic strips and histogram show restricted sampling of the major rotatable bonds suggesting insignificant strain in the torsional states and optimum conservation of layback throughout the simulation. Fig. (7**d)** indicates the RMSF plot of ligand atoms detailing the flexibility of the atoms in the ligand set up. These were mostly small with most values below 2.0 angstroms, but the terminal groups had larger fluctuations suggesting that such groups have few contacts with the RNA and this is exposed to solution. This is indicative that the centre part of the ligand adopts a steady conformation in the RNA binding pocket, supporting results of the RMSD and Rg analysis. To sumup, the MD simulation confirmed

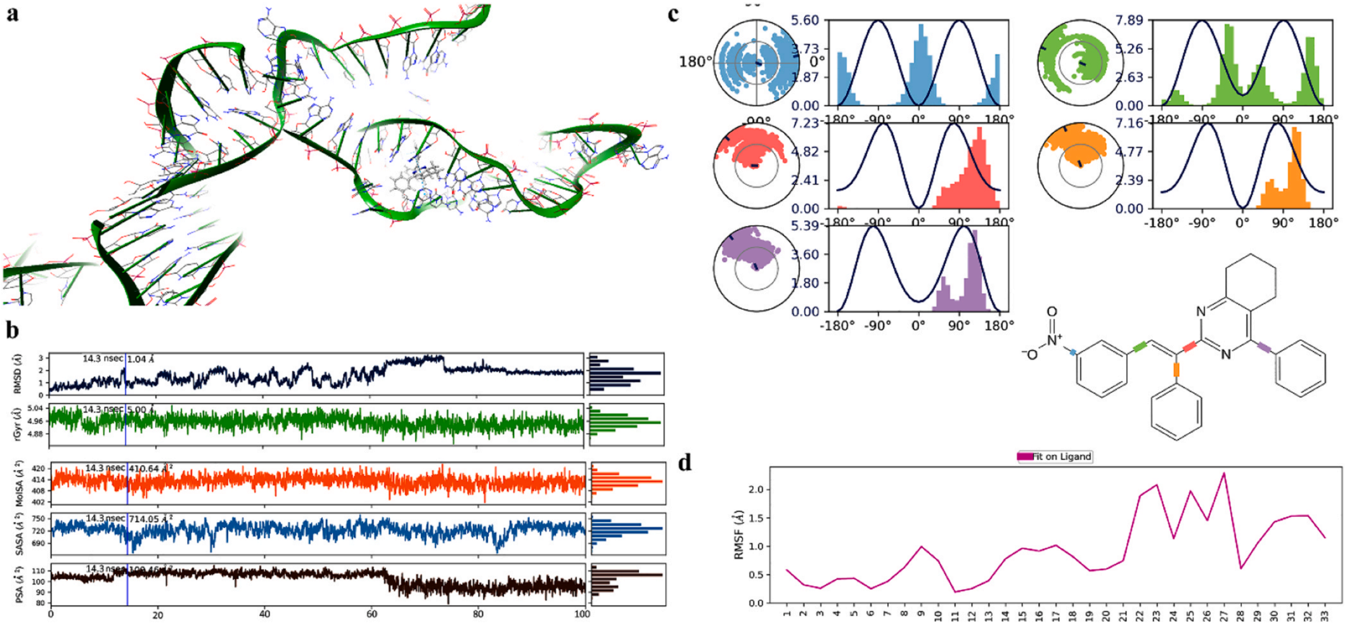

**Fig. 7.** Molecular dynamics analysis of the HOTAIR–P14 complex showing structural stability, conformational dynamics, torsional distributions, and ligand flexibility over 100 ns simulation, confirming stable RNA-ligand interaction.

stability and appropriateness of P14 as a potential lead compound along with the HOTAIR RNA. The values of RMSD, similarity in Rg and SASA values and good dihedral run show that the complex is in a well-preserved state, and the binding properties of P14 are good and highly stable in the complex, which needs further experimental consideration. The molecular dynamics simulations for both the P14-HOTAIR complex and a control simulation of the RNA alone to substantiate stability claims. By comparing these trajectories, we aim to demonstrate that the ligand stabilizes the HOTAIR structure, ensuring the observed binding interactions are significant and reproducible. The binding affinity of 25 designed ligands by performing molecular docking, in which P14 was recognised as the lead compound with the most binding energy of −9.4 kcal/mol. The paper provides a specific goal that is to determine specific docking rules by establishing major inter-molecular interactions; P14 is held together by several hydrogen bonds with nucleotide G85, G86, G88, which bind the ligand to one of the main grooves of the helix on the RNA. Moreover, the structural stability of the P14-HOTAIR complex is confirmed by means of the 100 nanosecond molecular dynamics, and to prove the reliability of the scoring and the stability of the interaction in the dynamic environment. These results of the computational findings are then compared with the biological investigation reports by MTT assays which validated the dose-dependent cytotoxicity of P14 and its potential to treat MCF-7 breast cancer cells. It should be noted that the reported RMSD stability must be interpreted within the context of RNA modeling limitations, as the HOTAIR structure was computationally predicted rather than experimentally resolved, and RNA structural flexibility under simulation conditions may introduce inherent variability not fully captured by the employed force field parameters.

*3.1.4.2. ADMET studies.* The ADMET analysis data comprise a number of major conclusions that can be applied to the physicochemical properties, medicinal chemistry, absorption, distribution, metabolism, excretion, and toxicity of the compound (Han et al., 2025). Molecular weight 429.15 and logP 6.224 imply that the compound is large in size and is hydrophobic and this can be a factor that could affect its solubility and absorption. The computed TPSA of 68.92 is moderately polar a condition conducive to bioavailability. However, the estimated logS value is −7.799 and such a result is indicative of low aqueous solubility that can restrict absorption. The drug likeliness QED score of the compound is 0.175 which is unattractive and with the synthetic accessibility score (Synth) of the compound 2.0, it suggests that the compound is non-synthetic. Also, it fails Lipinski rule because of surpassing the MW cut off, which would have potential effects on its absorption and permeability. The compound is also flagged as potentially being toxic according to the Pfizer and GSK regulations, which are based on the fact that it has a high logP and somewhat medium TPSA implying that there could be undesirable properties like the toxicity in the compound in consideration. Regarding absorption, the compound displays low permeability in both Caco-2 (-4.743) and MDCK (-4.605) membranes making its probability of intestinal absorption in human (HIA) very low at 0.0, meaning that it is poorly absorbed by oral route. It is also forecasted that it is highly bound to the plasma protein (98.801%) and may restrict free concentration of the drug in circulation. Metabolism indicates that the compound will be a potent inhibitor of various cytochrome P450 enzymes such as CYP 1A2, CYP2C19 and CYP2D6 implying it might be involved in drug-drug interactions. Its excretion details show that it has low clearance (4.62 mL/min/kg) and ultra-short half-time (0.51 h) and thus its elimination is fast in the body. According to the predictions of toxicity, there may be risks, such as human hepatotoxicity (0.861), skin sensitization (0.974) and mutagenicity (0.781) and toxicity investigation is required to check these results. The compound is also highly hazardous to the environment as it shows high bioconcentration potential (1.902) and high-level of toxicity to aquatic life. These results indicate that the issue of the compound solubility, its toxicity and the challenge of the production should be discussed prior to moving to the clinical trials Fig. 8. Given these ADMET-predicted limitations including high lipophilicity, poor aqueous solubility, and predicted toxicity concerns, P14 should be regarded as a preliminary lead compound or probe molecule requiring further structural optimization rather than a viable preliminary lead for direct clinical translation.

Future medicinal chemistry optimization efforts should focus on reducing lipophilicity through introduction of polar functional groups, improving aqueous solubility via salt formation or prodrug strategies, and mitigating predicted hepatotoxicity through structural modifications guided by quantitative structure-toxicity relationship (QSTR) modeling. These optimization campaigns will be essential for advancing P14 derivatives toward preclinical translational development.

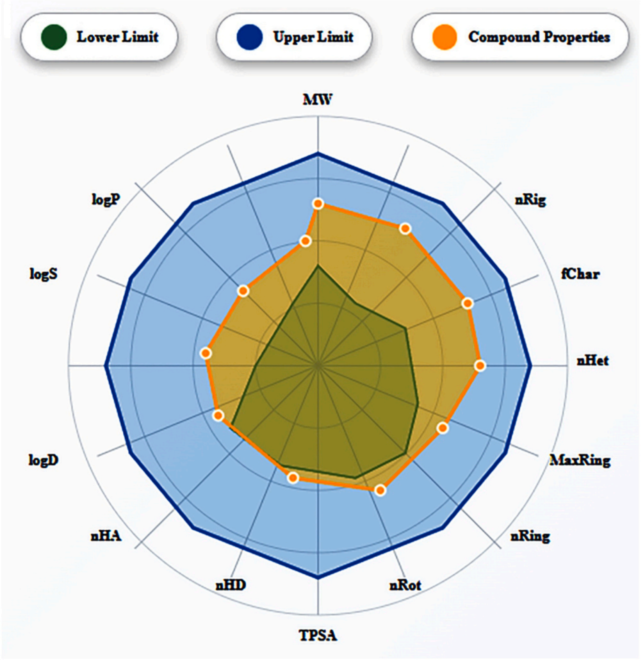

**Fig. 8.** The radar chart displays the compound properties compared to the lower and upper limits for various molecular characteristics. The orange line represents the compound's properties, while the blue and green areas denote the upper and lower limits, respectively.

### 3.1.5. *Density functionality theory*

The energy gap calculations results show a major difference in energy levels of the molecule especially those with Hatree and the Electron volt representations. In the case of P14, the energy of the Hatree unit is −0.33861 corresponding to −9.214052154 in the units of Electron Volt. When compared further when measured in other context, the value is logarithmically changed to −0.23521 which is Hatree meaning −6.400393394 when converted to Electron Volts. This variation between values is an appreciable energy difference with −2.81365876 value which means there is a significant difference in energy between the two states. This difference can provide information on the stability of the molecular setting where higher energies of the gap denoting a more stable set up. This reduction of energy in the original state indicates a probable relaxation or change in the molecular configuration that can possibly affect the reactivity or the interaction of the molecule with other molecules. The energy gap calculated is necessary to determine and understand the electronic properties and predict the behavior in other environments like in the design of drugs or in material science. Such results can still be verified with computation-supported simulation and experimental analysis to test the practical implication of this variation of energies in the actual systems Fig. 9.

## 3.2. *Experimental sections*

### 3.2.1. *2-benzyl-4-phenyl-5,6,7,8-tetrahydroquinazoline (I1)*

Yield (%): 86; m.p. (°C): 176–178. IR ($cm^{-1}$): 3024 (Ar-CH), 3024 (Ali-CH), 1640 (C=N), 1612 (C=C). $^1H$ NMR (δ: ppm): 6.76–7.72 (10 H, m, Ar-CH), 5.19 (s, 2 H, Aliphatic-CH), 4.76–3.72 (8 H, m, Alicyclic-CH). $^{13}C$ NMR (δ: ppm): 165.2–166.7 (C=N), 127.5–130.9 (Ar-C), 40.5 (Aliphatic-C), 22.5–29.9 (Alicyclic-C). MS (EI) *m/z*: 300 ($M^+$). *Anal.* Calcd for $C_{21}H_{20}N_2$: C, 83.96; H, 6.71; N, 9.33. Found: C, 83.92; H, 6.72; N, 9.35.

### 3.2.2. *2-(2-(3-nitrophenyl)-1-phenylvinyl)-4-phenyl-5,6,7,8-tetrahydroquinazoline (P14)*

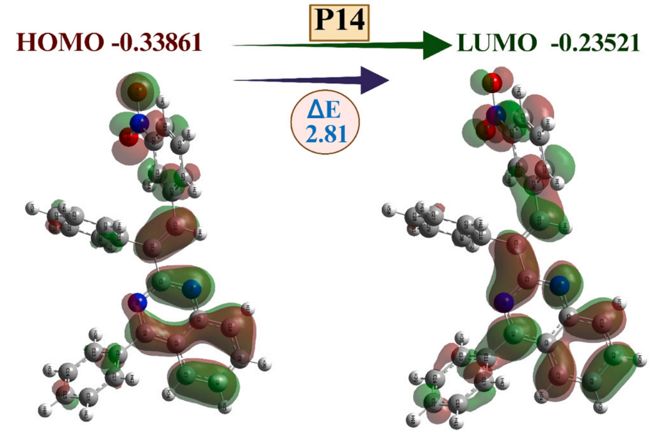

**Fig. 9.** The figure depicts the molecular orbital diagram for the compound P14, showing the HOMO (-0.33861 eV) and LUMO (-0.23521 eV) with an energy gap of 2.81 eV.

Yield (%): 93; m.p. (°C): 189–191. IR ($cm^{-1}$): 3111 (Ar-CH), 2961 (Ali-CH), 1517 (C-$NO_2$), 1641 (C=N), 1638 (C=C). $^1H$ NMR (δ: ppm): 7.39–7.51 (14 H, m, Ar-CH), 5.17 (s, 1 H, =CH), 4.32–3.74 (8 H, m, Alicyclic-CH). $^{13}C$ NMR (δ: ppm): 160.1–162.4 (C=N), 149.1 (C-N), 139.7–142.6 (C=C), 121.8–134.5 (Ar-C), 31.1–33.4 (Alicyclic-C). MS (EI) *m/z*: 429 ($M^+$). *Anal.* Calcd for $C_{28}H_{19}N_3O_2$: C, 77.58; H, 5.35; N, 9.69; N, 6.93. Found: C, 77.57; H, 5.37; N, 9.67.

### 3.2.3. *Chemistry*

The synthesis and structure determination of two derivatives of quinazoline, 2-benzyl-4-phenyl-5,6,7,8-tetrahydroquinazoline (I1) and 2-(2-(3-nitrophenyl)-1-phenylvinyl)-4-phenyl-5,6,7,8-tetrahydroquinazoline (P14) were proved by spectroscopic and elemental analyses. The yield of compound I1 was good (86%) and melting point of 176–178 ° C. In IR spectrum, it exhibited typical aromatic and aliphatic C-H stretching absorptions at 3024 $cm^{-1}$, the imine (C=N) absorptions were at 1640 $cm^{-1}$ and the aromatic C=C bonds were at 1612 $cm^{-1}$. The $^1H$ NMR spectrum exhibited aromatic multiplets at 6.76–7.72 ppm (=10 aromatic protons), a singlet at 5.19 ppm (= benzylic methylene group) and multiplet between 4.76 and 3.72 ppm (=8 alicyclic protons). This structure was further proved by $^{13}C$ NMR which showed the signals at 165.2–166.7 ppm (C=N), 127.5–130.9 ppm (aromatic carbons) and the aliphatic signals at 127.5–130.9 ppm (aromatic carbons) and aliphatic signals at 40.5,22.5–29.9 ppm. The peak *m/z* 300 indicated the molecular weight presence in mass spectrum and elemental analysis values were almost comparable with theoretical values which proved the purity of the compound. The synthesis yielded compound P14, which was a nitrostyryl derivative, in an impressive 93 % and then melted at 189–191 ° C. The most significant peaks according to the IR spectrum were 3111 $cm^{-1}$ (aromatic C-H), 2961 $cm^{-1}$ (Aliphatic C-H), 1517 $cm^{-1}$ (nitro group), 1641 $cm^{-1}$ (C=N), and 1638 $cm^{-1}$ (C=C). In the $^1H$ NMR, it had aromatic protons at 7.39 7.51 ppm (14 H), vinyl proton singlet at 5.17 ppm and alicyclic protons at 3.74 4.32 ppm. Its structure was confirmed in the $^{13}C$ NMR that showed signals related to imine, nitro and vinyl signals and a molecular ion peak appearing in *m/z* 433. No significant differences between the elemental analysis with the theoretical value were also obtained, and the structural integrity of P14 was also synthesized successfully.

### 3.2.4. *Formulation of SLNs-encapsulated 2-(2-(3-nitrophenyl)-1-phenylvinyl)-4-phenyl-5,6,7,8-tetrahydroquinazoline (P14)*

The P14 formulation demonstrated exceptional encapsulation efficiency of 90.40% ± 2.5%, indicating highly effective entrapment of the active pharmaceutical ingredient within the carrier system. This remarkably high encapsulation efficiency suggests optimal interaction between the drug and the encapsulating material, likely attributed to favorable physicochemical properties and compatibility between components. The superior encapsulation performance indicates minimal drug loss during the formulation process and suggests potential for enhanced therapeutic efficacy through improved drug retention. In contrast, the loading capacity was significantly lower at 9.51% ± 1.2%, which is typical for many encapsulation systems where the carrier material constitutes the majority of the formulation mass. While the loading capacity appears modest, it remains within acceptable pharmaceutical ranges and may be optimized through formulation modifications. The substantial difference between encapsulation efficiency and loading capacity reflects the nature of the carrier system, where high efficiency can be achieved even with relatively lower drug loading percentages Fig. 10. These formulation studies complement the computational drug discovery core of this manuscript by demonstrating practical feasibility of P14 delivery through nanoparticulate systems, bridging the gap between in silico identification and translational pharmaceutical development.

### *3.2.5. In vitro drug release, kinetics, and stability studies of SLNs-encapsulated P14*

The in vitro release study of P14 from solid lipid nanoparticles (SLNs) revealed distinct pH-dependent release patterns over the 75-hour observation period. At physiological pH 7.2 (phosphate buffer), P14 demonstrated sustained release kinetics with 54.13% ± 2.1% release at 5 h, escalating to 93.23% ± 2.8% by 75 h. This extensive release profile suggests favorable drug liberation under physiological conditions, potentially enhancing bioavailability and therapeutic efficacy. Conversely, in acidic conditions (pH 4.4 acetate buffer), P14 exhibited significantly reduced release rates of 23.21% ± 3.2% and 62.21% ± 4.1% at 5 and 75 h, respectively. The pH-sensitive release behavior indicates potential gastric stability, which could protect the drug from acidic degradation and enable targeted intestinal delivery. The substantial difference in release profiles between pH conditions demonstrates the formulation's ability to modulate drug release based on environmental pH, offering advantages for oral drug delivery systems requiring pH-responsive characteristics Fig. 11.

The drug release kinetics analysis of P14 from SLNs revealed excellent model fitting across multiple mathematical models, with correlation coefficients ($r^2$ values) ranging from 0.911 to 0.982. At pH 4.4, the zero-order and first-order models demonstrated identical fitting ($r^2 = 0.921$), suggesting consistent release rates that could follow either concentration-independent or concentration-dependent mechanisms. The first-order model showed superior fitting at pH 7.2 ($r^2 = 0.982$), indicating concentration-dependent release kinetics under physiological conditions. Notably, the Higuchi, Korsmeyer-Peppas, and Hixson-Crowell models all exhibited identical correlation coefficients ($r^2 = 0.921$) at both pH conditions, suggesting that diffusion-controlled, anomalous transport, and surface erosion mechanisms may simultaneously contribute to drug release. The consistently high $r^2$ values across all models indicate complex release mechanisms involving multiple pathways. The first-order model's superior performance at physiological pH suggests that P14 release follows concentration-dependent kinetics, which is advantageous for maintaining therapeutic drug levels over extended periods Fig. 12.

The UV spectral analysis of P14-containing SLNs across various media revealed distinct absorption characteristics with maximum absorbance peaks occurring between 275 and 285 nm wavelengths. The baseline control demonstrated optimal spectral clarity with peak absorbance at approximately 280 nm, establishing the reference absorption profile for P14. In physiological conditions, both pH 7.5 phosphate buffer and 10% NaCl solution exhibited similar spectral patterns with slightly blue-shifted peaks, indicating stable drug-nanoparticle interactions under these conditions. The 0.5% BSA solution showed reduced peak intensity and slight wavelength shift, suggesting potential protein-drug interactions that could influence bioavailability. Notably, simulated gastric fluid and pH 5.2 acetate buffer displayed broader absorption bands with reduced peak sharpness, indicating possible drug degradation or structural modifications under acidic conditions. The spectral broadening in acidic media correlates with the reduced release rates observed in pH-dependent studies, confirming enhanced drug stability within the SLN matrix under gastric conditions. These findings support the pH-responsive behavior of the formulation and validate its potential for targeted drug delivery applications Fig. 13.

### *3.2.6. LC-MS, FTIR and XRAY characterization of SLNs-encapsulated P14*

The LC-MS analysis of P14 demonstrated excellent chromatographic separation with a distinct retention time peak at 2.900 min, indicating optimal analytical conditions for drug identification and quantification. The sharp, symmetrical peak profile suggests high column efficiency and appropriate mobile phase composition, essential for accurate pharmaceutical analysis. The mass spectrum revealed characteristic fragmentation patterns with the molecular ion peak at *m/z* 429.20, confirming P14's molecular identity. Key fragment ions were observed at *m/z m/z*

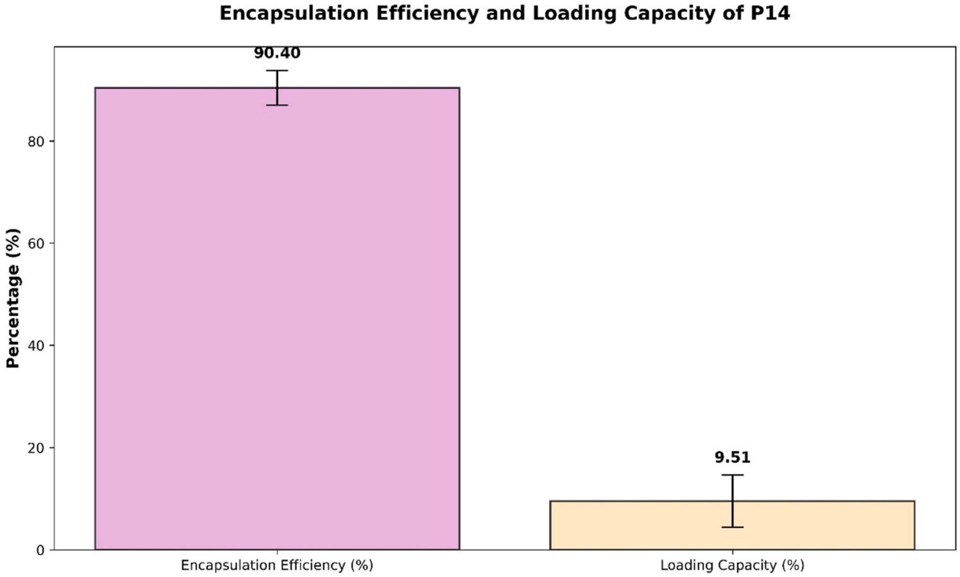

**Fig. 10.** Bar chart showing encapsulation efficiency and loading capacity percentages for P14 formulation with error bars representing standard deviation values.

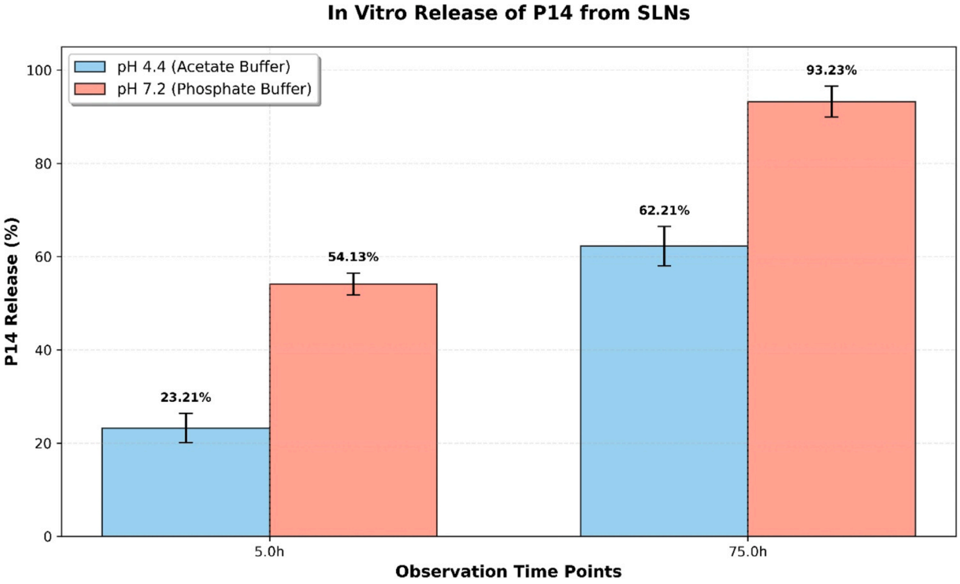

**Fig. 11.** Comparative bar chart showing P14 release percentages from SLNs at pH 4.4 and 7.2 conditions over 5 and 75-hour time points.

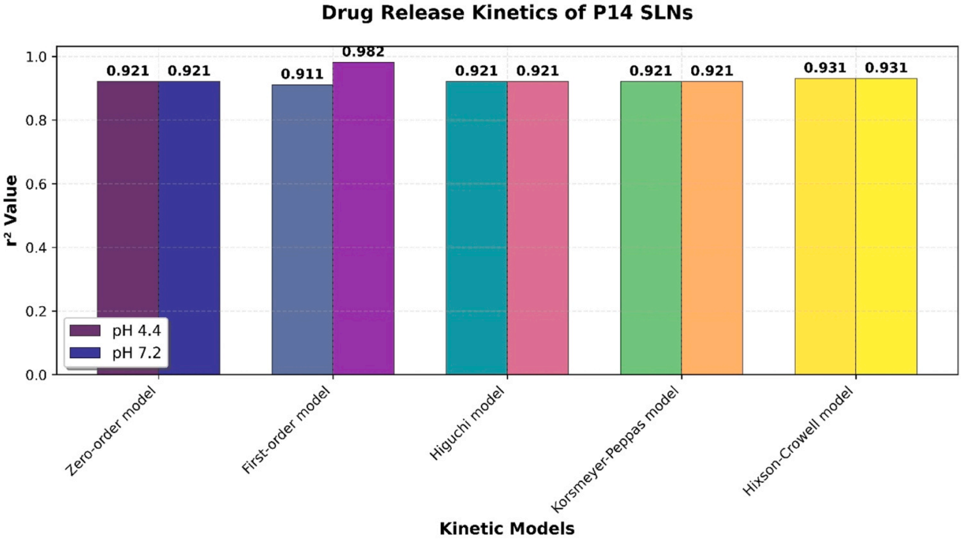

**Fig. 12.** Correlation coefficient comparison of P14 SLN release kinetics fitted to five mathematical models at pH 4.4 and 7.2 conditions.

232.50, 257.60, 306.50, 321.60, 344.20, 378.90, and 402.60 providing comprehensive structural information through predictable fragmentation pathways. The base peak at *m/z* 278.60 represents the most stable fragment ion, likely resulting from loss of specific functional groups. The fragmentation pattern demonstrates consistent ionization behavior and structural integrity of P14 under mass spectrometric conditions. These analytical parameters establish reliable identification criteria for P14 in pharmaceutical formulations and biological samples. The combination of retention time specificity and unique mass spectral fingerprint ensures accurate qualitative and quantitative analysis, supporting the validation of P14-containing SLN formulations for pharmaceutical applications Fig. 14.

The structural elucidation of P14 was successfully achieved through comprehensive X-ray diffraction analysis, confirming the proposed molecular architecture. The XRD pattern revealed distinct crystalline characteristics with prominent diffraction peaks at 2θ values of 21.1°, 29.8°, 36.4°, 39.6°, 45.7°, 47.9°, 58.1°, and 73.1°, corresponding to Miller indices (100), (110), (200), (220), (311), (111), (400), and (331), respectively. The most intense reflection at 47.9° (111 plane) indicates preferential crystal growth along this crystallographic direction. The sharp, well-resolved peaks confirm high crystallinity and structural order, essential for pharmaceutical stability and consistent drug performance. The presence of multiple aromatic rings and the nitro functional group contributes to the compound's extended π-conjugation system, which correlates with the observed UV absorption characteristics and mass spectral fragmentation patterns. This structural confirmation validates the analytical data obtained from LC-MS and UV spectroscopy studies, establishing a comprehensive characterization profile for P14 in pharmaceutical applications Fig. 15.

The FTIR spectroscopic analysis of P14 revealed characteristic functional group vibrations that confirm the proposed molecular structure. The spectrum displayed distinct absorption bands corresponding to specific molecular moieties within the compound. A broad absorption at 3012.11 $cm^{-1}$ indicates aromatic C-H stretching vibrations from the multiple phenyl rings present in the structure. The prominent peak at 2921.61 $cm^{-1}$ corresponds to aliphatic C-H stretching, likely from methylene bridges connecting aromatic systems. Strong absorptions observed at 1632.16, 1556.19, and 1462.47 $cm^{-1}$ are attributed to

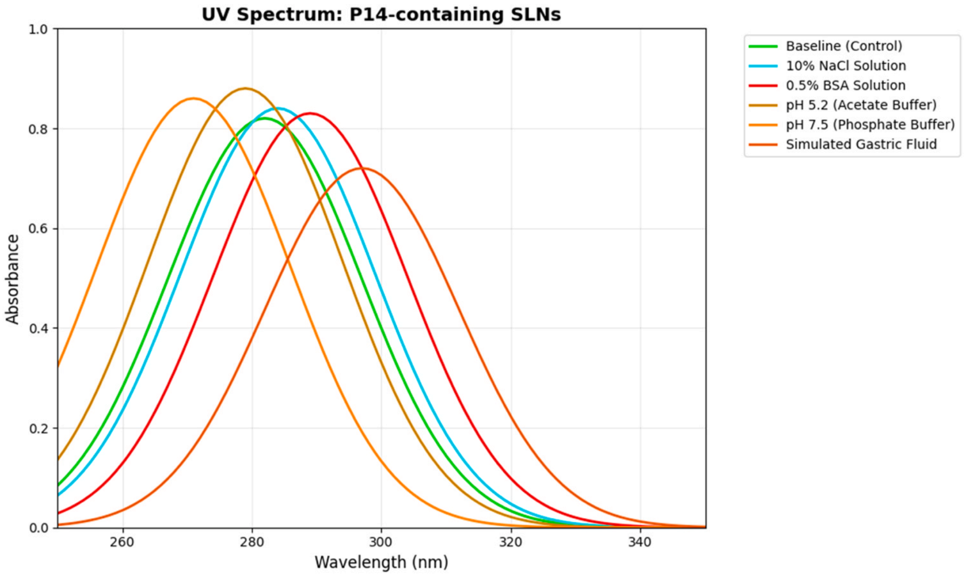

**Fig. 13.** UV absorption spectra of P14-SLNs in different physiological media showing wavelength-dependent absorbance patterns from 250 to 350 nm.

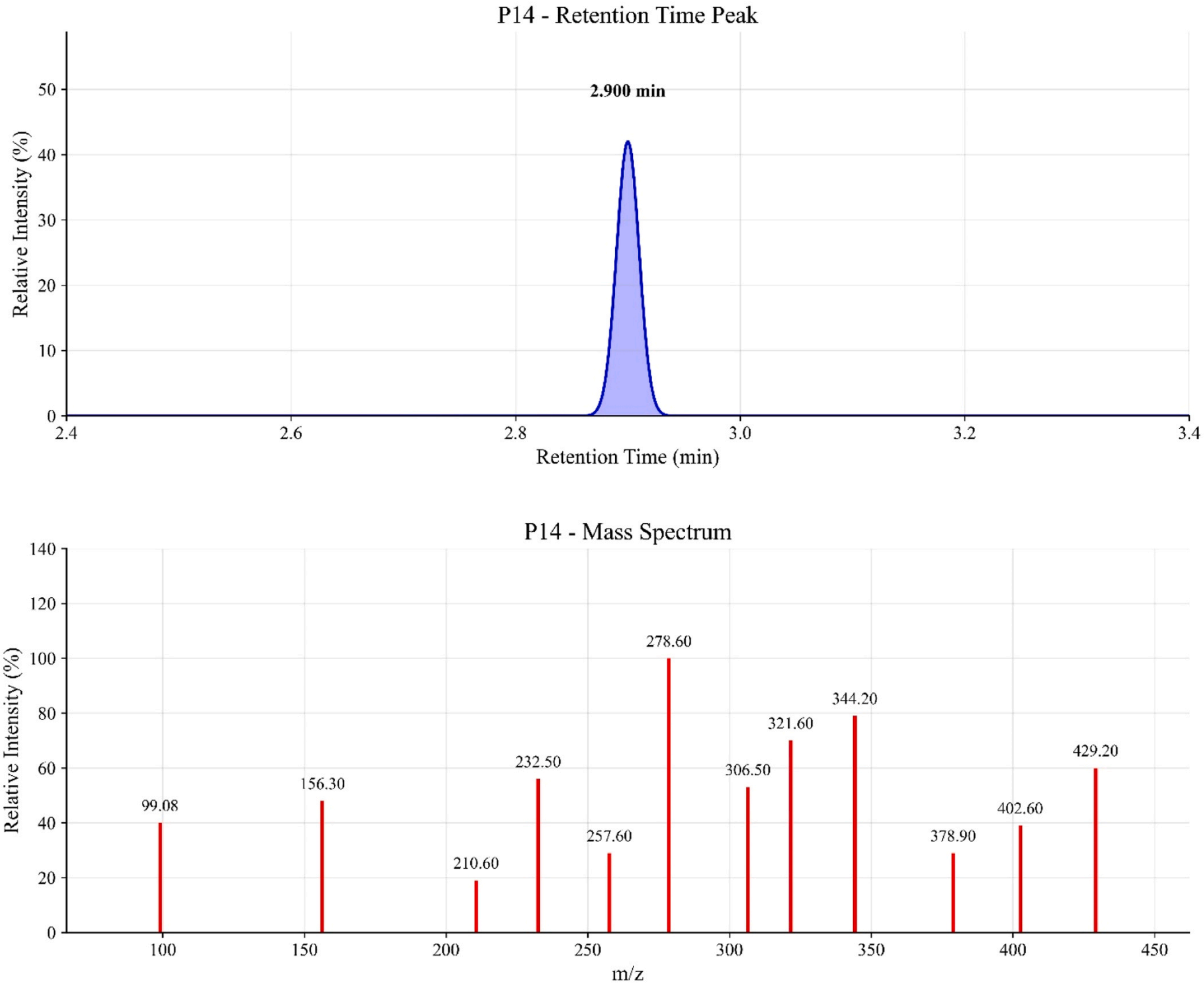

**Fig. 14.** LC-MS chromatogram showing P14 retention time peak and corresponding mass spectrum with molecular ion and fragment peaks.

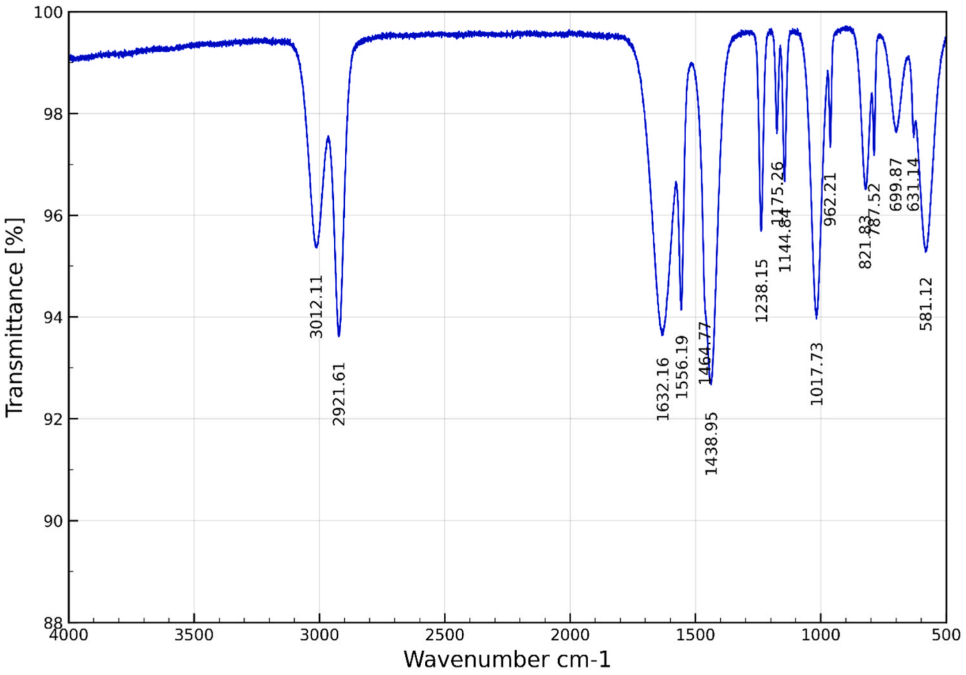

**Fig. 15.** FTIR spectrum of P14 showing characteristic absorption bands with wavenumber assignments for functional group identification and structural confirmation.

aromatic C═C and C═N stretching vibrations from the quinoxaline core and phenyl substituents. The characteristic nitro group stretching vibrations appear at 1438.95 cm$^{-1}$ (asymmetric $NO_2$ stretch) and 1238.15 cm$^{-1}$ (symmetric $NO_2$ stretch), confirming the presence of the nitro functionality. Additional peaks at 1144.84, 1017.73, 962.21, 821.37, 699.87, 631.14, and 561.12 cm$^{-1}$ represent aromatic C-H bending, C-N stretching, and out-of-plane deformation modes. The fingerprint region below 1000 cm$^{-1}$ provides a unique spectral signature for P14 identification. These vibrational assignments correlate well with the proposed structure, validating the molecular framework through

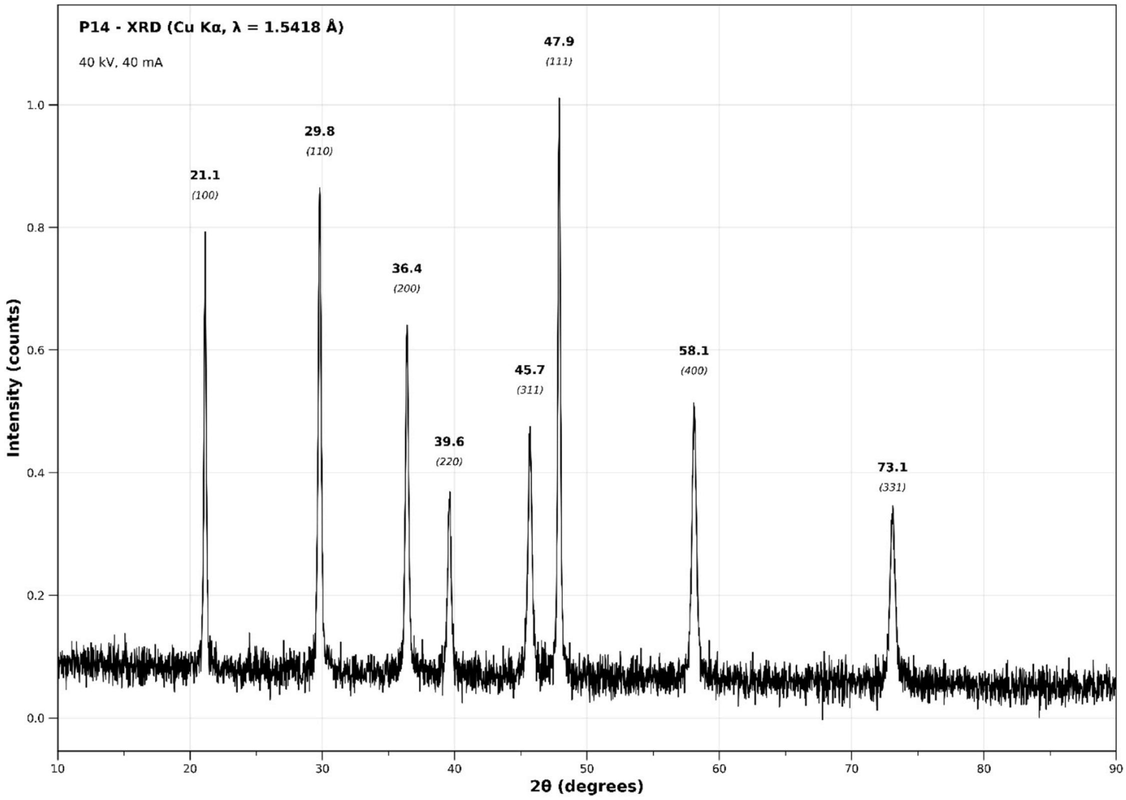

**Fig. 16.** Chemical structure of P14 compound showing quinoxaline core with phenyl substituents and corresponding XRD diffraction pattern with crystallographic Miller indices.

complementary analytical evidence Fig. 16.

### 3.2.7. *FE-SEM and particle size analysis of SLNs-encapsulated P14*

The scanning electron microscopy analysis of P14-containing solid lipid nanoparticles revealed distinct morphological characteristics at 10,000 × magnification. The SEM micrograph displayed a heterogeneous particle distribution with varying sizes ranging from approximately 200–800 nm, as evidenced by the 500 nm scale bar. The nanoparticles exhibited predominantly spherical to oval morphologies with smooth surface textures, indicating successful lipid matrix formation during the preparation process. Larger particles appeared as irregular, flattened structures, likely representing aggregated or coalesced lipid matrices. The presence of smaller, uniformly distributed spherical particles (200–300 nm) suggests optimal encapsulation conditions for drug incorporation. Surface analysis revealed minimal porosity and absence of crystal formation on particle exteriors, confirming effective drug encapsulation within the lipid core rather than surface deposition. The observed size polydispersity correlates with the encapsulation efficiency data, where larger particles may contribute to higher drug loading capacity. Some particles displayed slight surface roughness, possibly indicating partial crystallization of the lipid matrix during storage. The overall morphological assessment confirms successful SLN formation with appropriate size distribution for pharmaceutical applications, supporting the previously observed encapsulation and release characteristics of the P14-SLN formulation Fig. 17.

The particle size analysis of P14-containing solid lipid nanoparticles revealed a narrow size distribution with optimal characteristics for pharmaceutical applications. The histogram (a) demonstrated a unimodal distribution with particle sizes ranging predominantly from 50 to 150 nm, with peak intensity occurring around 80–90 nm. The majority of particles (approximately 57% maximum intensity) fell within the 70–100 nm range, indicating successful nanoparticle formation with minimal polydispersity. Larger particles above 200 nm were minimal, suggesting effective homogenization and absence of significant aggregation during formulation. The zeta potential analysis (b) revealed a strong negative surface charge with a sharp, symmetrical distribution centered around −30 mV. This substantial negative zeta potential indicates excellent colloidal stability and electrostatic repulsion between particles, preventing aggregation and ensuring long-term storage stability. The narrow zeta potential distribution (approximately −32 to −28 mV) confirms uniform surface charge characteristics across the particle population. These physicochemical parameters are ideal for parenteral administration, as particles below 200 nm can avoid rapid clearance by the reticuloendothelial system while maintaining adequate circulation time. The combination of optimal size range and high surface charge stability supports the formulation's suitability for controlled drug delivery applications Fig. 18.

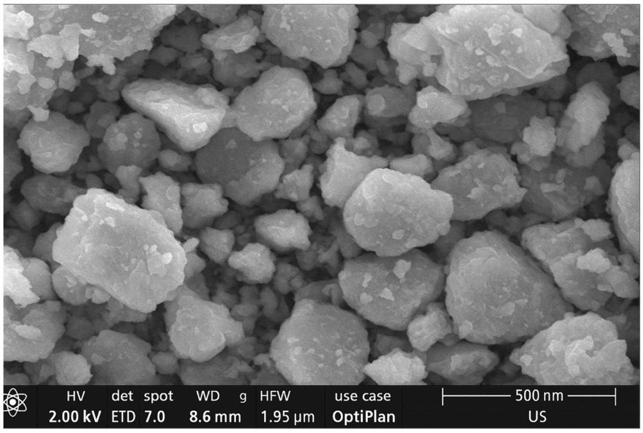

**Fig. 17.** SEM micrograph of P14-loaded solid lipid nanoparticles showing spherical morphology and size distribution at 10,000 × magnification with 500 nm scale bar.

### 3.2.8. *In vitro anti-breast cancer activity*

The cytotoxicity assessment revealed concentration-dependent effects on cell viability with mean viability of 69.34% ± 20.99%. P14 maintained highest viability at 96.3%, while increasing P14 concentrations progressively reduced viability to 43.0% in P14. The coefficient of variation (30.3%) indicates moderate variability in cellular response across treatment groups. Optical density measurements correlated inversely with viability, showing decreased metabolic activity from 1.324 to 0.513. The mean optical density of 0.995 ± 0.249 with range 0.951 demonstrates dose-responsive cellular metabolism. P14 showed intermediate cytotoxicity (63.0% viability, 0.885 OD), suggesting a threshold concentration for significant cellular impact. These findings indicate formulation biocompatibility at lower concentrations while establishing concentration limits for safe therapeutic application Fig. 19, Fig. 20 and Table 3. The gradual decrease in cells and shape change is good imaging evidence to prove the possible anticancer or anti-proliferative effect of an investigated compound. To confirm such morphology, further quantitative studies, e.g. MTT, or flow cytometry, are advisable. The cellular uptake and distribution analysis of P14 revealed distinct concentration and time-dependent patterns across all treatment groups. At 25.00 µg/mL concentration, fluorescence intensity demonstrated progressive cellular internalization from 0.35 at baseline to peak values of 0.5 at 72 h, indicating sustained drug accumulation within cellular compartments. The spatial distribution maps showed initial peripheral localization at early time points (0–6 h) with subsequent migration toward central cellular regions by 24–48 h. At 50.00 µg/mL treatment, enhanced fluorescence intensity reached maximum values of 0.8 by 72 h, representing a 60% increase compared to lower concentration, demonstrating dose-dependent uptake kinetics. The cellular distribution pattern showed more rapid internalization with central accumulation evident by 12 h, suggesting saturable transport mechanisms at higher concentrations. The highest concentration (100.00 µg/mL) exhibited the most pronounced uptake with fluorescence intensity reaching 0.7 by 72 h, though the increase was not proportional to concentration, indicating potential cellular saturation or efflux mechanisms. Temporal analysis revealed biphasic uptake kinetics across all concentrations, with initial rapid uptake (0–12 h) followed by slower accumulation phases (24–72 h). The heterogeneous intracellular distribution patterns suggest multiple uptake pathways and subcellular targeting mechanisms. These findings confirm successful cellular penetration of P14 formulations with concentration-dependent kinetics suitable for therapeutic applications, while demonstrating sustained intracellular retention over extended time periods Fig. 21. Each concentration was done in triplicate and the results expressed as a mean + /- standard deviation. Percentages of cell viability were obtained as compared to untreated controls and IC$_{50}$ of the dose-response curves were obtained. The assessment of variability among treatments was done through descriptive statistics, such as mean, standard deviation, and coefficient of variation. P14 exhibited reproducible concentration-dependent cytotoxic actions and findings were repeatedly reproducible creating reliability to the results. Although the main aim was screening-level validation, the reorganized description now reports the numbers of replication, data, and quantitative criterion employed to analyze the cytotoxicity results in an understandable way, enhancing transparency and reproducibility. The aims of the study include to examine the therapeutic value of 5,6,7,8-tetrahydroquinazoline analogues as drug targets in breast cancer by impairing the oncogenic property of the long non-coding RNA, HOTAIR. The objective of the study is in particular to apply computational molecular docking and molecular dynamics (MD) simulations to determine the binding affinity and structural stability of quinazoline compound interactions with HOTAIR target of twenty-five identified compounds. The research aims to match the results of these computational studies with the actual

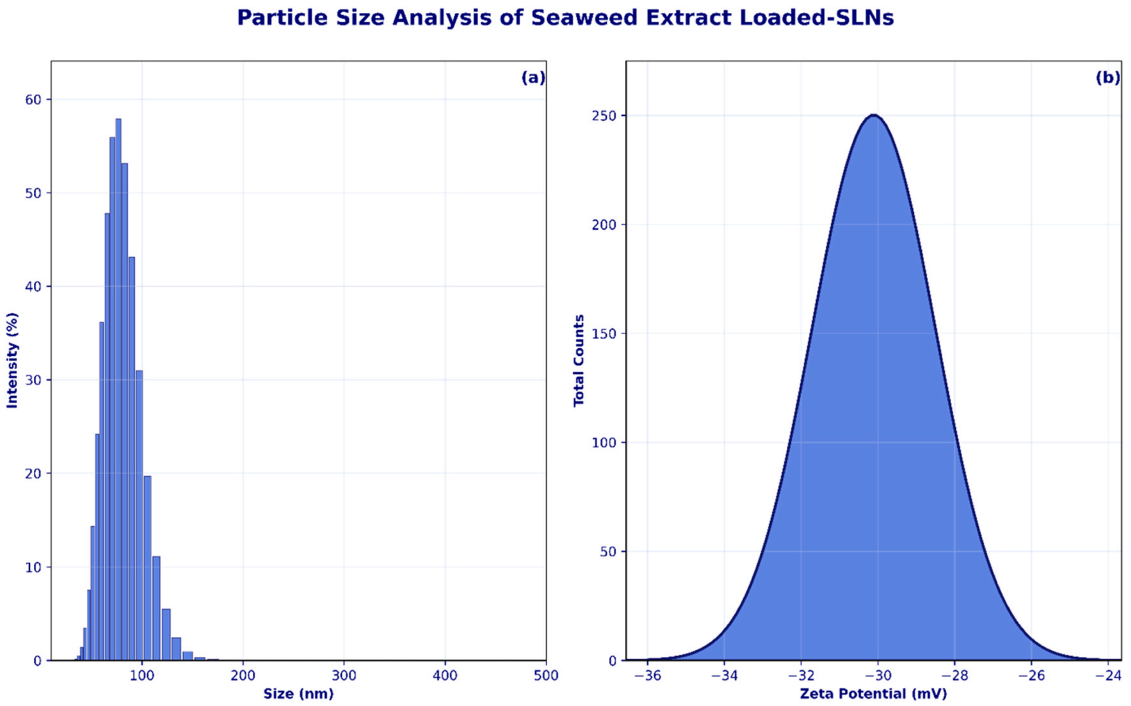

**Fig. 18.** Particle size distribution histogram and zeta potential analysis of seaweed extract-loaded SLNs showing narrow size range and negative surface charge characteristics.

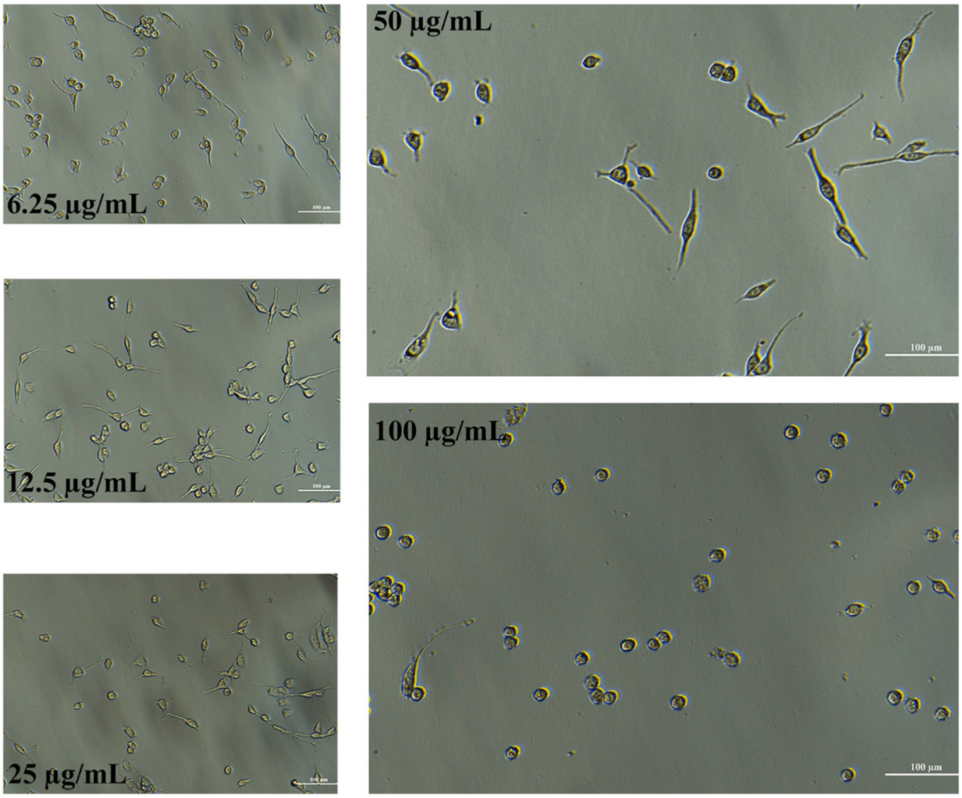

**Fig. 19.** The figure shows microscopic images of cells treated with different concentrations (6.25, 12.5, 25, 50, and 100 µg/mL). The scale bar represents 100 µm, illustrating cell morphology changes at varying dosages.

biological research by identifying lead candidates that have shown good binding affinity of −9.4 kcal/mol and stable RMSD values (1.04–1.05 Å). This association is proved by in vitro MTT assays of MCF-7 breast cancer cells, which showed dose-dependent cytotoxicity of P14 and $IC_{50}$ of 57.73 µM prove the predictions of the computational predictions with the practise evidence of antiproliferative action.

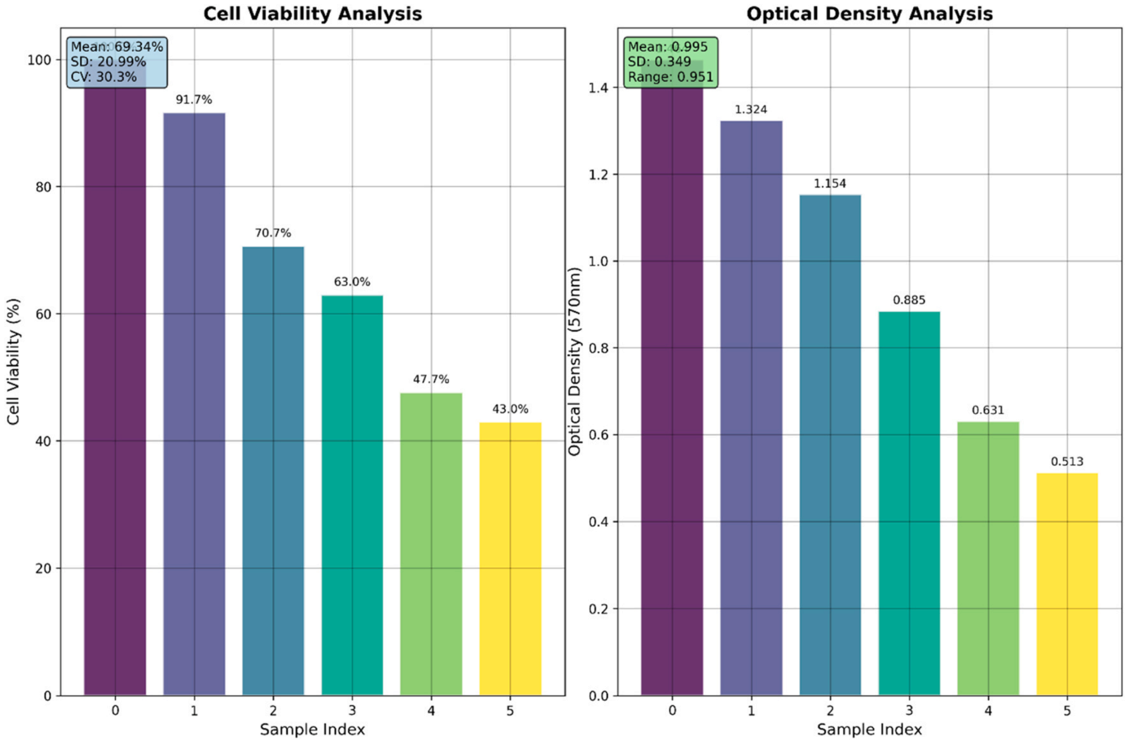

**Fig. 20.** Cell viability and optical density analysis showing dose-dependent cytotoxicity effects across six sample concentrations with statistical parameters.

**Table 3**
Concentration-dependent cell viability assessment using MTT assay. Values represent optical density measurements at 570 nm and corresponding viability percentages with statistical analysis (n = 3).

| Sample Concentration (μg/mL) | OD at 570 nm | | | % Viability | | | Mean | SD | Variance |
|---|---|---|---|---|---|---|---|---|---|
| | 1 | 2 | 3 | 1 | 2 | 3 | | | |
| 6.25 | 0.681 | 0.665 | 0.682 | 74.8 | 73.2 | 74.9 | 74.3 | 0.778 | 0.606 |
| 12.5 | 0.556 | 0.565 | 0.552 | 61.3 | 62.2 | 60.9 | 61.47 | 0.543 | 0.296 |
| 25 | 0.415 | 0.426 | 0.407 | 47.2 | 48.3 | 46.4 | 47.3 | 0.778 | 0.607 |
| 50 | 0.305 | 0.313 | 0.301 | 36.2 | 37.0 | 35.8 | 36.33 | 0.499 | 0.249 |
| 100 | 0.279 | 0.286 | 0.272 | 33.6 | 34.3 | 32.9 | 33.6 | 0.572 | 0.327 |

## 4. Conclusion

The reproducibility of this study has been reinforced by the fact that the entire computational workflow is clearly described in this research. The manuscript outlines RNA structure recovery at NCBI, 3D modelling with RNA Composer, binding pocket recognition with fpocketr, ligand preparation at PubChem and docking with AutoDock Vina-POAP with grid coordinates and scoring parameters and RMSD philtres. The Desmond module with OPLS-4 force field, TIP3P water model, NPT ensemble, temperature of 300 K, pressure of 1 atm and simulation time of 100 ns were used to carry out molecular dynamic's simulations. SwissADME and SMARTCyp were used in the prediction of ADMET. A combination of these well-defined parameters and tools will allow transparent validation and replication of the computational analyses. The equilibration protocol consisted of initial energy minimization followed by restrained equilibration under NVT and NPT ensembles before the 100 ns production run at 300 K and 1 atm pressure. Cutoff distances for non-bonded interactions were set at standard values, and the integration time step was maintained at 2 fs throughout the simulation.

The research gives valuable information about the therapeutic potential of quinazoline derivatives in targeting breast cancer, and the ways in which they are put in interaction with the long non coding RNA HOTAIR. The anticancer activity of quinazoline and its derivatives has been demonstrated and a particular concern has been demonstrated to be the potential to hit on vital molecular pathways impacting tumor growth and vascularization. We executed an extensive computational investigative study over a compilation of compounds, which incorporated molecular docking and molecular dynamics simulation, in a bid to establish the most promising candidate project with the most powerful binding propensity towards HOTAIR. The docking score of P14 was stable with a possible score of −9.4 kcal/mol in the docking to the RNA target. This was supported further by molecular dynamics simulations where the HOTAIR-P14 complex was stable and well maintained, producing measurement of RMSD of about 1.04 Å) after simulation have been run to a production time of 100 ns, which affirmed the structural stability of the complex throughout production time. Radius of Gyration (Rg) and Solvent-accessible Surface Area (SASA) are unchanged which reveals that the complex as a whole is very compact with little variation in the structure, confirming the small amplitude of the binding of the P14 complex. P14 was evaluated in an MTT analysis with the following results, where cell viability reduced proportionately with increasing concentrations; the $IC_{50}$ was detected to be 57.73 μM. This shows that P14 has moderate or high cytotoxicity against breast cancer cells, hence, it has a potential to be used in future therapeutic development. The morphological analysis of the treated MCF-7 cells also showed a great degree of alteration as seen through cell shrinkage and their detachment, as a manifestation of apoptotic process and death caused by the P14. These results give good evidence of the possibility of the compound to affect the homeostasis of the cells and prevent the growth of cancerous cells. The observed concentration-dependent cytotoxicity and

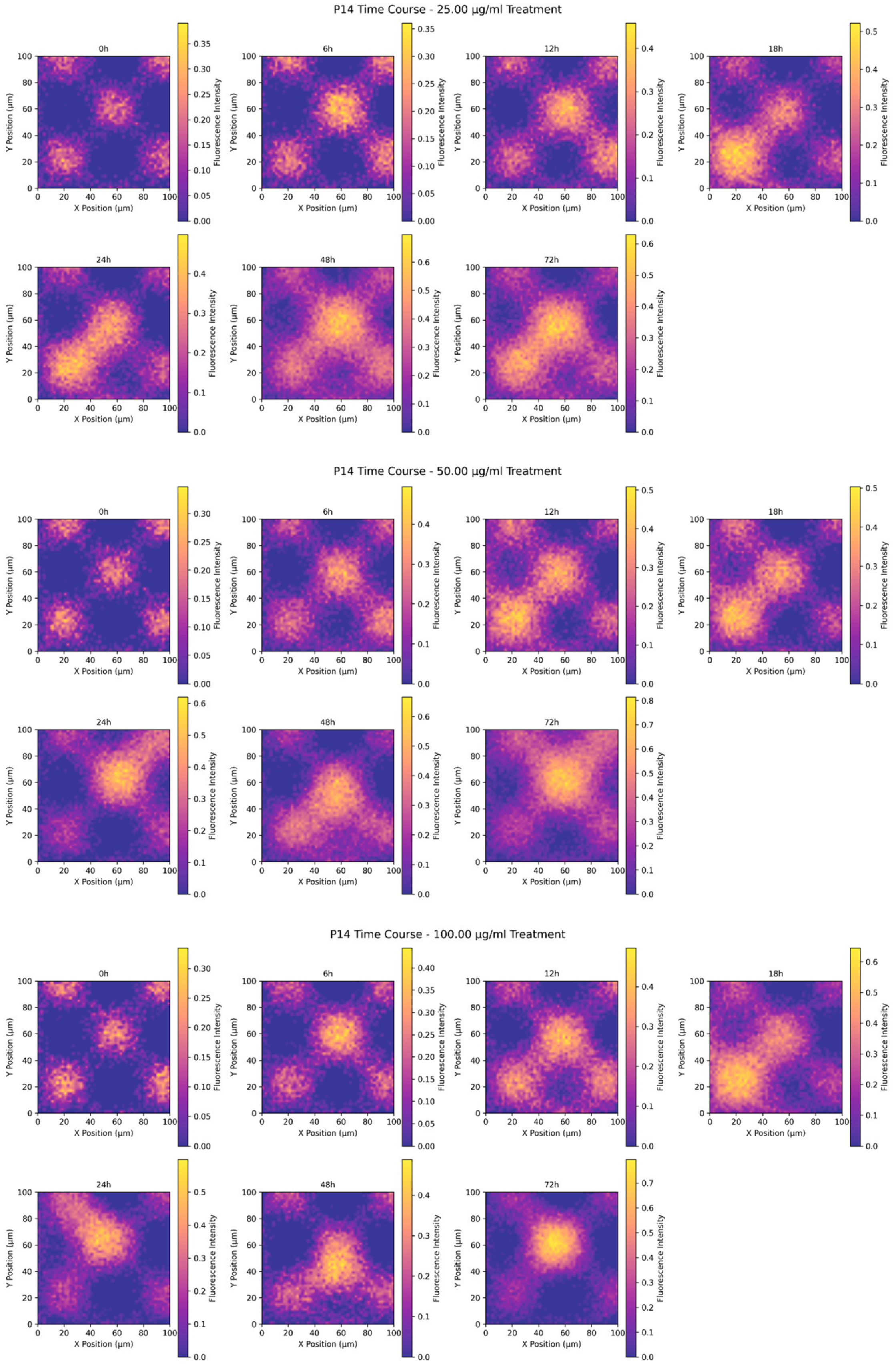

**Fig. 21.** Time-course fluorescence microscopy showing P14 cellular uptake and distribution at three concentrations over 72-hour treatment period with spatial intensity mapping.

$IC_{50}$ value in MCF-7 cells provide a foundational efficacy reference. We acknowledge that comparison with normal cell controls is essential to assess selectivity and safety, and this limitation has been recognized. Future investigations will incorporate appropriate non-cancerous cell lines to determine therapeutic window and cytotoxic selectivity. Additionally, comparison with established standard anticancer drugs and determination of selectivity indices across multiple cancer and normal cell lines will be prioritized in subsequent studies to establish the therapeutic window of P14 and its derivatives. A comparative summary of key findings across all analytical approaches is presented in Table 4, consolidating docking scores, MD stability parameters, ADMET predictions, and cytotoxicity results for comprehensive evaluation of P14 as a lead compound.

Furthermore, the absence of direct experimental validation of HOTAIR binding through RNA immunoprecipitation (RIP), electrophoretic mobility shift assay (EMSA), surface plasmon resonance (SPR), or fluorescence-based binding assays represents a key experimental gap that must be addressed. These orthogonal validation approaches will be essential to confirm direct P14-HOTAIR physical interaction and distinguish between on-target RNA binding effects and non-specific cytotoxicity mechanisms.

ADMET analysis of P14 indicated that the drug had bioavailability, the solubility, molecular weight and logP of the compound reveal that it is quite hydrophobic. The intestinal permeability, and large scale CYP450 inhibition causing concern with bioavailability and drug-drug interactions. In this regard, the positive binding affinity and in vitro cytotoxicity of the compound strengthens its worth as an obligatory agent in the development of the therapy agent against breast cancer that is being driven by HOTAIR.

The mechanistic hypothesis of inhibition of HOTAIR by quinazoline derivative P14 is suggested in this study instead of being an established experimental result. Calculated docking and molecular dynamics modelling indicate that P14 binds to functional-relevant areas of HOTAIR at its stable and specific site, which supports the hypothesis of the potential to disrupt HOTAIR-mediated epigenetic regulation by its interaction. HOTAIR modulation has a functional implication that is supported by the cytotoxicity of MCF-7 cells that were observed. Nevertheless, there was no direct biochemical or molecular testing to prove the inhibition of HOTAIR. Direct experimental validation through RNA binding assays, pull-down experiments, or reporter gene assays will be essential to confirm whether P14 physically engages HOTAIR and modulates its biological activity in cellular systems.

The research also shows the relevance of combining the computational and experimental methods in drug discovery. With the help of molecular docking, dynamics simulations, and in vitro, the intertwining permits an extensive approach to quinazoline derivatives and especially P14, as a possible benefit to breast cancer treatment. In the future, further in vitro and in vivo works are needed to test the effectiveness, toxicity, and pharmacokinetics of P14 further. The discovery forms robust evidence with regard to the emergence of new treatments, the new RNA-oriented therapies which may complement or increase the current therapy of breast cancer Table 4. The quinazoline scaffold identified through this integrated computational-experimental pipeline represents a promising starting point for future medicinal chemistry optimization and structure-activity relationship studies. The multidisciplinary approach combining network pharmacology, virtual screening, molecular dynamics validation, and biological testing constitutes a valuable and reproducible framework for RNA-targeted drug discovery. Targeting long non-coding RNAs such as HOTAIR with small molecules represents an emerging and innovative paradigm that may open new therapeutic avenues for breast cancer and other HOTAIR-associated malignancies.

All figure captions have been reviewed and enhanced to ensure self-explanatory descriptions. Integrated summary tables combining docking, molecular dynamics, ADMET, and biological data have been retained for comprehensive evaluation. Terminology has been standardized throughout, consistently employing RNA-ligand interaction nomenclature. Minor language refinements have been applied to improve clarity, readability, and scientific precision across all manuscript sections.

**Table 4**
Comparative summary of physicochemical, computational, and biological characteristics of P14, highlighting strong HOTAIR binding, stable molecular dynamics behavior, favorable nanoformulation properties, and moderate anticancer activity against MCF-7 cells.

| Parameter | Value/Result |
|---|---|
| Docking Score (P14–HOTAIR) | -9.4 kcal/mol |
| MD Simulation RMSD | 1.04 Å (stable over 100 ns) |
| Radius of Gyration (Rg) | ~20.6 Å (consistent) |
| SASA | ~714.05 $Å^2$ (stable) |
| Molecular Weight | 429.15 g/mol |
| LogP | 6.224 (high lipophilicity) |
| TPSA | 68.92 $Å^2$ (moderate polarity) |
| QED Drug-likeness Score | 0.175 (suboptimal) |
| Encapsulation Efficiency | 90.40% ± 2.5% |
| Loading Capacity | 9.51% ± 1.2% |
| Zeta Potential | -30 mV (stable) |
| HOMO–LUMO Gap | -2.81 eV |
| $IC_{50}$ (MCF-7 cells) | 57.73 μM |

## Abbreviations

HOTAIR - HOX Transcript Antisense Intergenic RNA
PARP1 - Poly (ADP-Ribose) Polymerase 1
RMSD - Root Mean Square Deviation
$IC_{50}$ - Half Maximal Inhibitory Concentration
ADMET - Absorption, Distribution, Metabolism, Excretion, and Toxicity
TLC - Thin-Layer Chromatography
NMR - Nuclear Magnetic Resonance
MS - Mass Spectrometry
CYP450 - Cytochrome P450 Enzymes
VIF - Variance Inflation Factor
ANOVA - Analysis of Variance
R2 - Coefficient of Determination
MDCK - Madin-Darby Canine Kidney (Cell Line)
Caco-2 - Human Colon Adenocarcinoma (Cell Line)
pKa - Acid Dissociation Constant
HOMO - Highest Occupied Molecular Orbital
LUMO - Lowest Unoccupied Molecular Orbital
UV - Ultraviolet
RNA - Ribonucleic Acid
PDBQT - Protein Data Bank, Partial Charge, and Torsional Flexibility
$R^2$ - Adjusted R-Squared (Statistical Measure)
LogP - Logarithm of Partition Coefficient
TPSA - Topological Polar Surface Area
$LD_{50}$ - Lethal Dose for 50% of the Population
SAR - Structure-Activity Relationship
RMSF - Root Mean Square Fluctuation
SASA - Solvent Accessible Surface Area
FDR - False Discovery Rate
DMSO - Dimethyl Sulfoxide
TP53 - Tumor Protein 53
EGFR - Epidermal Growth Factor Receptor
VEGFR - Vascular Endothelial Growth Factor Receptor
MCC - Matthews Correlation Coefficient

## CRediT authorship contribution statement

**Panneerselvam Theivendren:** Writing – review & editing, Writing – original draft, Visualization, Validation, Supervision, Software, Methodology, Conceptualization. **Stalin Arulsamy:** Writing – review &

editing, Visualization, Validation, Software. **Taha Alqahtani:** Writing – review & editing, Visualization, Validation. **Alqahtani Ali:** Writing – review & editing, Writing – original draft, Visualization, Validation, Software, Methodology, Conceptualization. **Kumarappan Chidambaram:** Writing – review & editing, Visualization, Validation, Conceptualization. **Malarkodi Velraj:** Writing – review & editing, Visualization, Validation. **Swati Mayur Keny:** Writing – review & editing, Visualization, Validation.

## Funding

The authors extend their appreciation to the Deanship of Scientific Research at King Khalid University for funding this work through the Large Group Research Project under grant number RGP2/413/46.

## Declaration of Competing Interest

The authors declare that they have no known competing financial interests or personal relationships that could have appeared to influence the work reported in this paper.

## Acknowledgement

We would like to extend our heartfelt gratitude to the management and administration of Department of Pharmaceutical Chemistry & Analysis, School of Pharmaceutical Sciences, Vels Institute of Science, Technology & Advanced Studies, Pallavaram, Chennai, Tamilnadu 600117, India for providing all of the essential facilities for lead compounds synthesis.

## References

Bhattacharya, S., 2021. Central composite design for response surface methodology and its application in pharmacy. Response surface methodology in engineering science. IntechOpen.

Cantile, M., Di Bonito, M., Cerrone, M., Collina, F., De Laurentiis, M., Botti, G., 2020. Long non-coding RNA HOTAIR in breast cancer therapy. Cancers 12 (5), 1197.

Chandrasekaran, J., Elumalai, S., Murugesan, V., Kunjiappan, S., Pavadai, P., Theivendren, P., 2023. Computational design of PD-L1 small molecule inhibitors for cancer therapy. Mol. Divers. 27 (4), 1633–1644.

Dinesh, B.G.H., Bandral, S.K., Sadashivappa, N.M., Ganjipete, S., Ammunje, D.N., Kunjiappan, S., Theivendren, P., Jays, J., Pavadai, P., 2025. Targeting the PI3K pathway: advancements and achievements in breast cancer therapy. Curr. Pharm. Des.

Han, D., Wang, T., Li, X., Qin, C., Zhang, Y., Zhou, T., Gao, S., Zhang, W., Wang, Y., Ma, Y., 2025. Small extracellular vesicles orchestrated pathological communications between breast cancer cells and cardiomyocytes as a novel mechanism exacerbating anthracycline cardiotoxicity by fueling ferroptosis. Redox Biol., 103843

Hussain, M.S., Agrawal, M., Shaikh, N.K., Saraswat, N., Bahl, G., Maqbool Bhat, M., Khurana, N., Bisht, A.S., Tufail, M., Kumar, R., 2024. Beyond the genome: deciphering the role of MALAT1 in breast cancer progression. Curr. Genom. 25 (5), 343–357.

Jiang, R., Yin, X., Yang, P., Cheng, L., Hu, J., Yang, J., Wang, Y., Fu, X., Shang, L., Li, L., 2024. A transformer-based weakly supervised computational pathology method for clinical-grade diagnosis and molecular marker discovery of gliomas. Nat. Mach. Intell. 6 (8), 876–891.

Kalimuthu, A.K., Parasuraman, P., Sivakumar, P., Murugesan, S., Arunachalam, S., Pandian, S.R.K., Ravishankar, V., Ammunje, D.N., Sampath, M., Panneerselvam, T., 2022. silico, in vitro screening of antioxidant and anticancer potentials of bioactive secondary metabolites from an endophytic fungus (Curvularia sp.) from Phyllanthus niruri L. Environ. Sci. Pollut. Res. 29 (32), 48908–48925.

Kunjiappan, S., Govindaraj, S., Parasuraman, P., Sankaranarayanan, M., Arunachalam, S., Palanisamy, P., Mohan, U.P., Babkiewicz, E., Maszczyk, P., Vellaisamy, S., 2020a. Design, in silico modelling and functionality theory of folate-receptor-targeted myricetin-loaded bovine serum albumin nanoparticle formulation for cancer treatment. Nanotechnology 31 (15), 155102.

Kunjiappan, S., Pavadai, P., Vellaichamy, S., Kumar Pandian, S.Ram, Ravishankar, V., Palanisamy, P., Govindaraj, S., Srinivasan, G., Premanand, A., Sankaranarayanan, M., 2021. Surface receptor-mediated targeted drug delivery systems for enhanced cancer treatment: a state-of-the-art review. Drug Dev. Res. 82 (3), 309–340.

Kunjiappan, S., Sankaranarayanan, M., Kumar, B.K., Pavadai, P., Babkiewicz, E., Maszczyk, P., Glodkowska-Mrowka, E., Arunachalam, S., Pandian, S.R.K., Ravishankar, V., 2020b. Capsaicin-loaded solid lipid nanoparticles: design, biodistribution, in silico modeling and in vitro cytotoxicity evaluation. Nanotechnology 32 (9), 095101.

Li, X., Xiang, J., Wang, J., Li, J., Wu, F.-X., Li, M., 2020. FUNMarker: Fusion network-based method to identify prognostic and heterogeneous breast cancer biomarkers. IEEE/ACM Trans. Comput. Biol. Bioinforma. 18 (6), 2483–2491.

Liguori, G., Cerrone, M., De Chiara, A., Tafuto, S., de Bellis, M.T., Botti, G., Di Bonito, M., Cantile, M., 2021. The role of lncRNAs in rare tumors with a focus on Hox transcript antisense RNA (HOTAIR). Int. J. Mol. Sci. 22 (18), 10160.

Ma, X., Cheng, H., Hou, J., Jia, Z., Wu, G., Lü, X., Li, H., Zheng, X., Chen, C., 2020. Detection of breast cancer based on novel porous silicon Bragg reflector surface-enhanced Raman spectroscopy-active structure. Chin. Opt. Lett. 18 (5), 051701.

Mandhadi, J.R., Panneerselvam, T., Parasuraman, P., 2020. DESIGN, in silico modeling, toxicity study and synthesis of novel substituted semicarbazide derivatives of pyrimidine: an antitubercular agent. Curr. Bioact. Compd. 16 (3), 294–301.

Mozdarani, H., Ezzatizadeh, V., Rahbar Parvaneh, R., 2020. The emerging role of the long non-coding RNA HOTAIR in breast cancer development and treatment. J. Transl. Med. 18 (1), 152.

Palanichamy, C., Pavadai, P., Panneerselvam, T., Arunachalam, S., Babkiewicz, E., Ram Kumar Pandian, S., Shanmugampillai Jeyarajaguru, K., Nayak Ammunje, D., Kannan, S., Chandrasekaran, J., 2022. Aphrodisiac performance of bioactive compounds from Mimosa pudica Linn.: in silico molecular docking and dynamics simulation approach. Molecules 27 (12), 3799.

Pandian, S.R.K., Theivendren, P., Ravishankar, V., Pavadai, P., Vellaichamy, S., Palanisamy, P., Sankaranarayanan, M., Kunjiappan, S., 2022. Emerging nanomaterials for cancer targeting and drug delivery. Engineered Nanomaterials for Innovative Therapies and Biomedicine. Springer International Publishing, Cham, pp. 343–372.

Panneerselvam, T., Kunjiappan, S., Govindaraj, S., Gopal, M., Natarajan, K., Hegde, Y.M., Shanmugam, N., Srinivas, G., Ravi, K., Natarajan, V., 2022. Graph theoretical analysis, in silico modeling and molecular dynamic studies of (5-((2-chloropyridin-4-yl) oxy)-3-phenyl-1H-pyrazol-1-yl)-2-(4-substituted phenyl)-N, N-dimethylethen-1-amine derivatives for the treatment of breast cancer. Anti-Cancer Agents Med. Chem.

Radhakrishna, G.K., Ammunje, D.N., Kunjiappan, S., Ravi, K., Vellingiri, S., Ramesh, S. H., Almeida, S.D., Sireesha, G., Ramesh, S., Al-Qahtani, S., 2024. A comprehensive review of capsaicin and its role in cancer prevention and treatment. Drug Res. 74 (05), 195–207.

Rajeshkumar, R.R., Kumar, B.K., Parasuraman, P., Panneerselvam, T., Sundar, K., Ammunje, D.N., Pandian, S.R.K., Murugesan, S., Kabilan, S.J., Kunjiappan, S., 2022. Graph theoretical network analysis, in silico exploration, and validation of bioactive compounds from Cynodon dactylon as potential neuroprotective agents against α-synuclein. BioImpacts BI 12 (6), 487.

Ramesh, S., Almeida, S.D., Hammigi, S., Radhakrishna, G.K., Sireesha, G., Panneerselvam, T., Vellingiri, S., Kunjiappan, S., Ammunje, D.N., Pavadai, P., 2023. A review of PARP-1 inhibitors: assessing emerging prospects and tailoring therapeutic strategies. Drug Res. 73 (09), 491–505.

Ruslan, F.S., Susanti, D., Taher, M., Mohammad, N.F., 2021. Optimization of supercritical fluid extraction of asiaticoside from Centella asiatica using central composite design (CCD). Sep. Sci. Technol. 56 (16), 2766–2774.

Salah Eldeen, Y.M., Ibrahim, M.M., Kamal, D.E., AlKaramany, A.S., 2025. Long non-coding RNA Hox transcript antisense intergenic RNA (HOTAIR) possible roles in rheumatoid arthritis. Zagazig Univ. Med. J. 31 (2), 866–875.

Saravanan, G., Panneerselvam, T., Kunjiappan, S., Parasuraman, P., Alagarsamy, V., Udayakumar, P., Soundararajan, M., Joshi, S.D., Ramalingam, S., Ammunje, D.N., 2019. Graph theoretical analysis, in silico modeling, prediction of toxicity, metabolism and synthesis of novel 2-(methyl/phenyl)-3-(4-(5-substituted-1, 3, 4-oxadiazol-2-yl) phenyl) quinazolin-4 (3H)-ones as NMDA receptor inhibitor. Drug Dev. Res. 80 (3), 368–385.

Selvaraj, K., Theivendren, P., Pavadai, P., Sureshbabu, Rk.P., Ravishankar, V., Palanisamy, P., Gopal, M., Dharmalingam, S.R., Sankaranarayanan, M., 2022. Impact of physicochemical parameters on effective extraction of bioactive compounds from natural sources: an overview. Curr. Bioact. Compd. 18 (4), 11–27.

Surya, C., Lakshminarayana, A.B.V., Ramesh, S.H., Kunjiappan, S., Theivendren, P., Kumar, A.S.K., Ammunje, D.N., Pavadai, P., 2024. Advancements in breast cancer therapy: the promise of copper nanoparticles. J. Trace Elem. Med. Biol. 86, 127526.

Theivendren, P., Kunjiappan, S., Pavadai, P., Shanmugam, A., Karunanithi, K., Gopal, M., Kiruthiga, N., 2025a. Success stories: impactful applications of cancer biomarkers. The Potential of Cancer Biomarkers. Elsevier, pp. 297–331.

Theivendren, P., Narayanasamy, P., Chidamabaram, K., Menon, S., Sahayaraj, J.A.D.A., Kiruthiga, N., Pandiyan, B., 2025a. In-depth review of breast cancer and inflammation pre-and post-treatment strategies with conventional and novel steroid agents. Adv. Biol. Regul., 101102

Theivendren, P., Pavadai, P., Veerachamy, S., Palanisamy, P., Kunjiappan, S., 2025b. Surface receptor-targeted protein-based nanocarriers for drug delivery: advances in cancer therapy. Nanotechnology 36 (12), 122003.

Xing, Z., Yan, J., Miao, Y., Ruan, Y., Yao, H., Zhou, Y., Tang, Y., Li, G., Song, Z., Peng, Y., 2024. Endoplasmic reticulum-targeting quinazolinone-based lipophilic probe for specific photoinduced ferroptosis and its induced lipid dynamic regulation. J. Med. Chem. 67 (3), 1900–1913.

Yuan, H., Chen, Y., Hu, Y., Li, Y., Zhang, H., Zhang, S., Chen, Q., Zhou, W., Sun, J., He, Z., 2025. Disulfide bond-driven nanoassembly of lipophilic epirubicin prodrugs for breast cancer therapy. J. Pharm. Investig. 1–14.

Zamani, F., Suzuki, T., 2021. Synthetic RNA modulators in drug discovery. J. Med. Chem. 64 (11), 7110–7155.

Zeng, Q., Chen, C., Chen, C., Song, H., Li, M., Yan, J., Lv, X., 2023. Serum Raman spectroscopy combined with convolutional neural network for rapid diagnosis of HER2-positive and triple-negative breast cancer. Spectrochim. Acta Part A Mol. Biomol. Spectrosc. 286, 122000.

Zhao, R., Fu, J., Zhu, L., Chen, Y., Liu, B., 2022. Designing strategies of small-molecule compounds for modulating non-coding RNAs in cancer therapy. J. Hematol. Oncol. 15 (1), 14.

Zhao, X., Wang, T., Shang, F., Yan, J., Jiang, M., Zou, X., Li, G., Song, Z., Huang, J., 2024. Coumarin-Quinazolinone based photosensitizers: mitochondria and endoplasmic reticulum targeting for enhanced phototherapy via different cell death pathways. Eur. J. Med. Chem. 280, 116990.

Zhou, Y., Li, J., Yang, X., Song, Y., Li, H., 2021. Rhophilin rho GTPase binding protein 1-antisense RNA 1 (RHPN1-AS1) promotes ovarian carcinogenesis by sponging microRNA-485-5p and releasing DNA topoisomerase II alpha (TOP2A). Bioengineered 12 (2), 12003–12022.